NON-SYMMETRIC EDGE SPREAD FUNCTION IN NEUTRON RADIOGRAPHY

by

JEREMIAH CHUKWUECHEFULAM OSUWA, B.Sc. (Ife)

PART A: McMaster (on-campus) Project

A Report
Submitted to the School of Graduate Studies
in Partial Fulfillment of the Requirements for
the Degree
Master of Engineering

McMaster University
1979

One of two project reports: The other part is designated as Part B

MASTER OF ENGINEERING (1979) McMASTER UNIVERSITY
Department of Engineering Physics Hamilton, Ontario

TITLE: Non-Symmetric Edge Spread Function in Neutron Radiography

AUTHOR: J.C. Osuwa, B.Sc. (Ife)

SUPERVISOR: Dr. A.A. Harms

NUMBER OF PAGES: viii, 56

ABSTRACT

A combined experimental and theoretical investigation was carried out with neutron scattering samples to study the effect of scattering on the edge spread function.

A physically based mathematical formulation of the neutron processes in radiographic specimen in which scattering is dominant was found to be in good agreement with experimental results. In addition to full integral description for the edge-spread function, a generalized Lorentzian function has been proposed as an alternative method of analysis.

ACKNOWLEDGEMENT

The author wishes to thank Dr. A.A. Harms, Department of Engineering Physics, for his useful guidance in this research project. Appreciation is also extended to Mr. Mike Butler for his assistance in computing and to Miss Janet Delsey for typing this project report.

LIST OF FIGURES

LIST OF FIGURES (cont'd)

LIST OF TABLES

TABLE OF CONTENTS

CHAPTER 1

INTRODUCTION

The current application of neutron radiography in such important areas as dimensional measurements of radioactive nuclear fuel pins[1], and in accessing the condition of hidden machine parts clearly demonstrates the need for a higher precision in the attainable image sharpness[2]. Development of any technique for such precision measurements requires among other things, the consideration of edge effects for which neutron radiographers already focused attention on the discernment of the exact location of the edge of a radiographed knife edge sample. The problem posed here is that of optical density spread about the edge which takes an S-shape form when scanned with a microdensitometer thus rendering the edge visually inaccessible.

Up to date, reports have successfully accounted for this optical density spread across the edge by the use of the edge spread function[3,5] (ESF), which gives a symmetric S-shape curve connecting two regions of lower and higher optical densities. This, however, is the case only if the radiographed object is predominantly a neutron absorbing material. In the case when the object is a neutron scatterer, or when the ratio of the scattering cross-section to absorption cross-section of the material is appreciable, the edge spread function becomes non-symmetric. This scattering effect needs to be incorporated in the development of any reliable dimensional measurement technique in neutron radiography.

In the investigation that follows, a concerted effort has been made to obtain in as much simplified form as possible a mathematical formulation to account for the physical processes leading to this non-symmetry. The approach takes as a starting point, the already established form of the symmetric edge spread function and seeks to find some perturbation flux due to the neutrons scattered in the radiographed object. The total flux reaching any point on the converter inside the neutron camera is thus the sum of the scattered flux and the unscattered flux.

The total flux incorporated with the Lorentzian function can be integrated to obtain the desired edge spread function as in the symmetric case. However, unlike the symmetric case, the integration of the flux with the Lorentzian function is analytically intractable due to the form which the scattered flux assumes. The alternative is then to resort to numerical computation to obtain the desired result. The problem becomes more involved by the presence of double integration for which numerical approaches are still on the developing stage.

The attainment of the end result presented in this report, has been greatly enhanced by the use of the only existing computer library programme for double integration at McMaster University - DCS2QU[4] - a two dimensional cubic spline quadrature.

In order to simplify the formulation, only the case of single scattering has been considered in this presentation, and it is hoped that cases involving multiple scattering can be accounted for by the inclusion of build up factor in the analysis. To obtain experimental results which are consistent with the single scattering treatment, the dimensions of the radiographed lucite samples are chosen so as to reduce the effect of multiple scattering.

CHAPTER 2

EXPERIMENTAL PROCEDURES AND RESULTS

2.1 A Review of Symmetric Edge Spread Function

As a brief review, we shall present the form which the edge spread function takes in the case when no scattering of neutrons occurs in the radiographed sample.

It is generally known that the symmetric edge spread function $S(x,\alpha)$ is related to a line-spread function, $L(x,\alpha)$ by a dual integral-differential equation[5]

$$L(x,\vec{\alpha}) = N^{-1} \frac{d}{dx} S(x,\vec{\alpha}) \tag{2.1}$$

$$S(x,\vec{\alpha}) = N \int_{-\infty}^{x} L(\xi,\vec{\alpha})d\xi \tag{2.2}$$

where for a given radiographic system, $\vec{\alpha}$ is a vector characterised by film type, energy of source, converter material etc., and N is a normalisation constant usually chosen such that $S(x,\vec{\alpha}) \rightarrow \{0,1\}$ as $x \rightarrow \{-\infty,\infty\}$.

Taking $\vec{\alpha}$ for the system as a dispersion parameter C_L, known as the Lorentzian coefficient, the Lorentzian line-spread function is then given by

$$L(x,C_L) = \frac{1}{1 + C_L x^2} \tag{2.3}$$

In this case, the edge spread function can be reduced analytically to the form

$$S(x,c) = N \int_{-\infty}^{x} \frac{d\xi}{1 + C\xi^2} = \frac{1}{2} + \frac{1}{\pi} \tan^{-1}(x\sqrt{c}) \tag{2.4}$$

where N has taken on the normalization value $\sqrt{c}/\pi$, and the integration limit goes from $-\infty$ to the point x about where the edge is located. The incident flux ϕ_o has also been taken to be unity, i.e.

$$L(x,c) = \frac{\phi_o}{1 + Cx^2} \longrightarrow \frac{1}{1 + Cx^2} \tag{2.5}$$

The edge-spread function given by equation (2.4) actually represents the converter response[6] to a unit incident flux which is assumed to be totally absorbed in the region of the sample while the flux reaches the converter unattenuated in the region with no object to intercept the neutron beam. Figure 2.1 shows the schematic form of the most common neutron radiographic system presently in use and identified as the back converter arrangement.

Neutrons reaching the converter give rise to secondary radiations[1,6] which are emitted isotropically from any point u, say, on the converter, and the converter response measured at any point x on the film is obtained by using the Lorentzian function in the form

$$L(x,u) = \frac{1}{1 + C(x-u)^2} \tag{2.6}$$

where x-u, is the distance measured from the edge of the object.

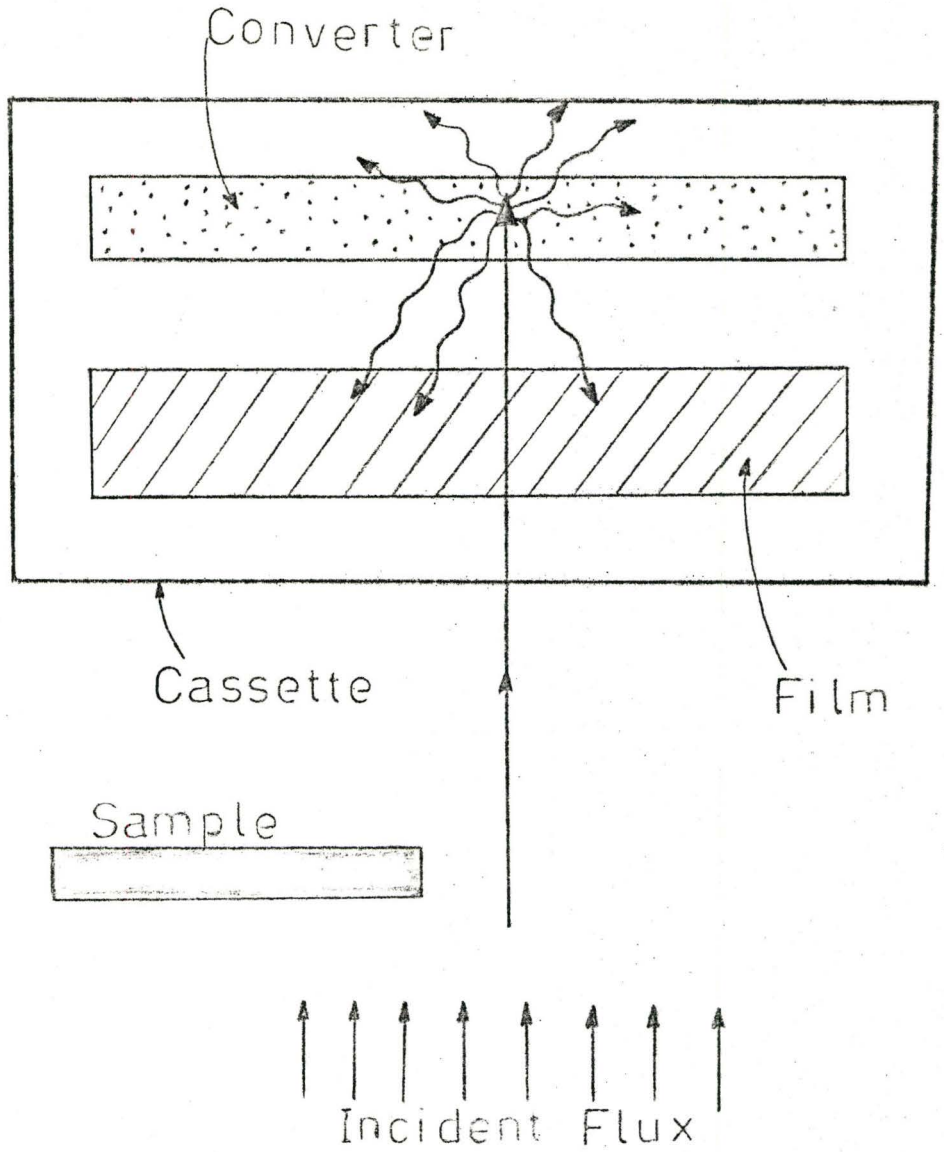

Fig. 2.1: A back converter arrangement showing neutron induced secondary radiations emitted isotropically about the point of neutron absorption.

2.2 Experimental Procedure

Several pieces of lucite samples with thicknesses ranging from 0.3 cm to 1.2 cm were thoroughly machined to give smooth and straight edges.

The choice of the sample was motivated by its high hydrogen and carbon contents which give the desired scattering effect. Lucite has a scattering cross-section of 0.2429 cm^{-1} as compared to absorption cross-section of 0.01913 cm^{-1}, giving a scattering to absorption cross-section ratio of 12.7:1.

The radiographic system used is the standard cassette type as shown in Figure 2.1 with gadolinium converter and Kodak AA film. The source of neutrons is a vertical beam port of a reactor which gives a flux of about 10^5n cm^{-2} s^{-1}. The radiographed knife edges were placed as close to the centre of the neutron beam as possible to reduce any effect that might be due to beam divergence. Some of the samples were radiographed three different times with different exposures of 4 minutes, 6 minutes and 8 minutes in order to determine the effect of exposure time on the ESF.

2.3 Results of Experiments

The scans obtained for the lucite samples using a densitometer, clearly show a deviation from symmetry in the ESF. For a given thickness of the lucite samples, the shape of the non symmetric ESF remains the same irrespective of the exposure time, as shown in Fig. 2.2 - Fig. 2.11; but for different thicknesses, different non-symmetric shapes are obtained depicting the extent of scattering that occured.

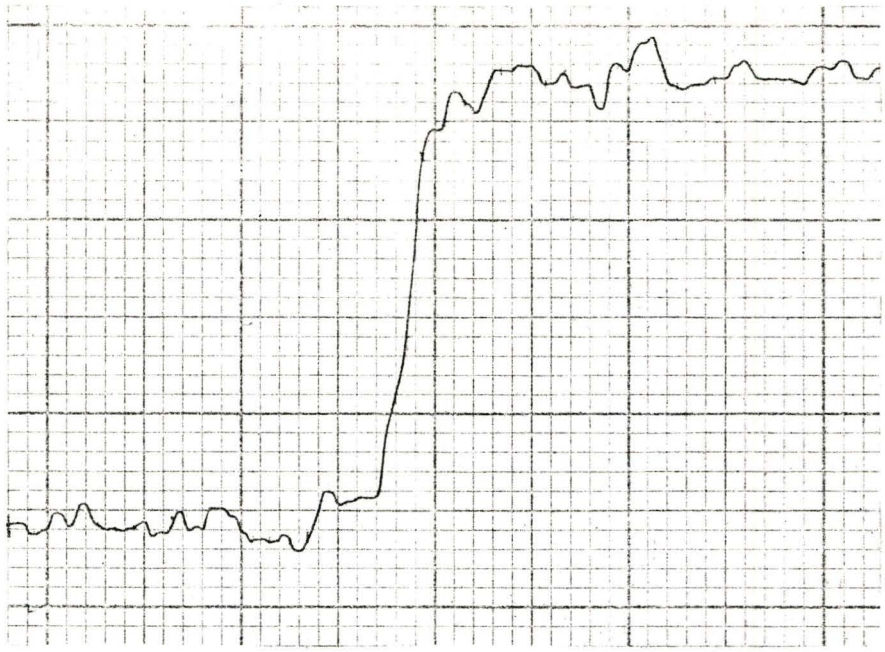

Fig. 2.2: Non-symmetric optical density scan for 0.3 cm thick lucite sample, exposed to standard neutron flux for 4 minutes.

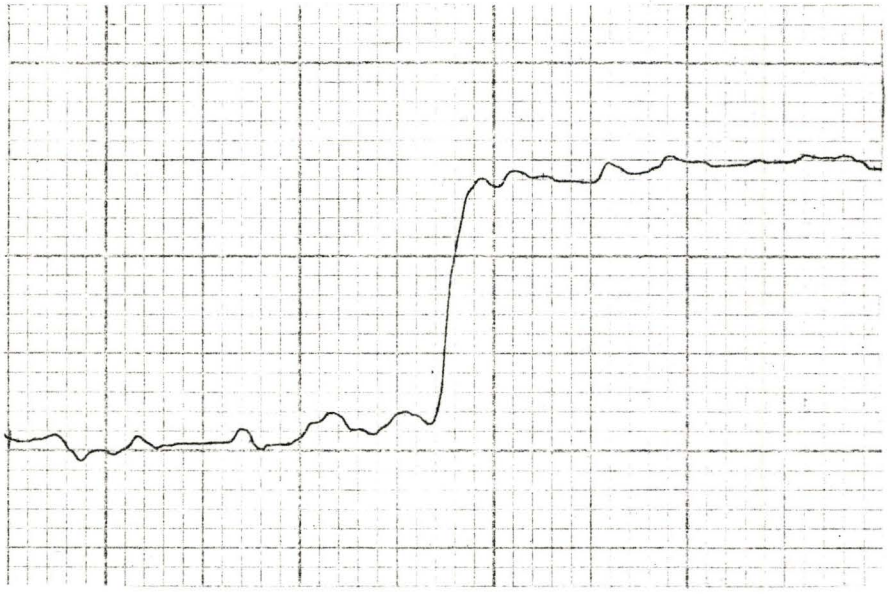

Fig. 2.3: Non-symmetric optical density scan for 0.3 cm thick lucite sample, exposed to standard neutron flux for 6 minutes.

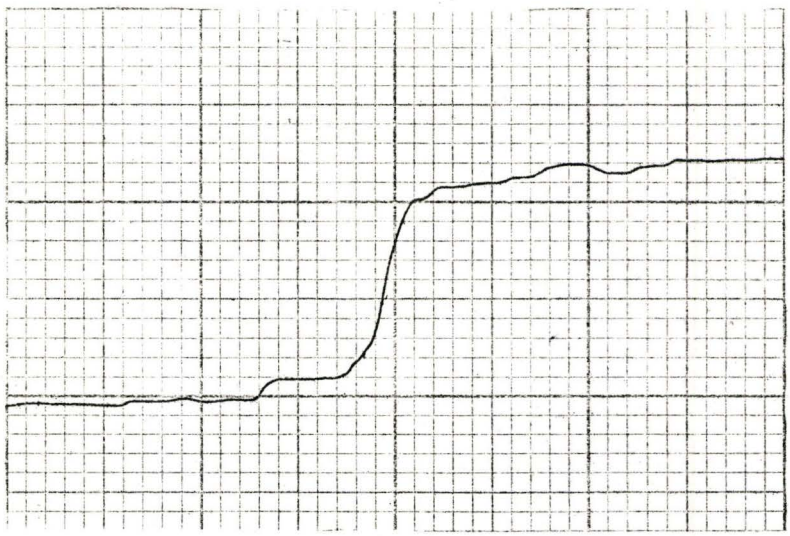

Fig. 2.4: Non-symmetric optical density scan for 0.5 cm thick lucite sample, exposed to standard neutron flux for 4 minutes.

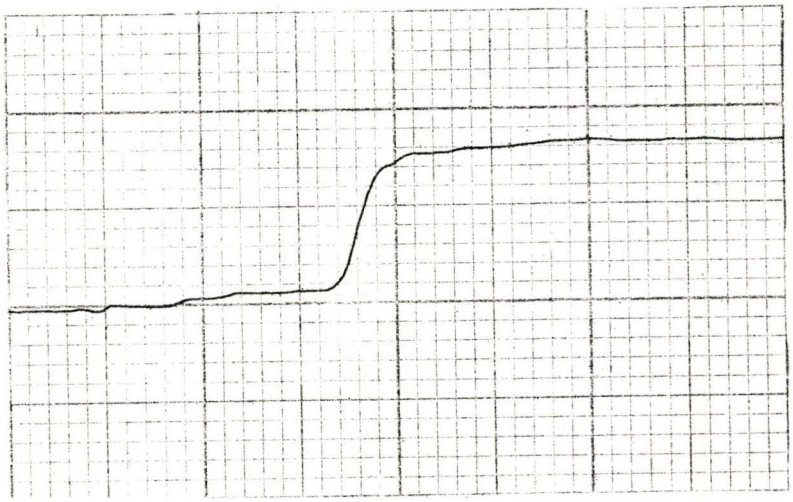

Fig. 2.5: Non-symmetric optical density scan for 0.5 cm thick lucite sample, exposed to standard neutron flux for 6 minutes.

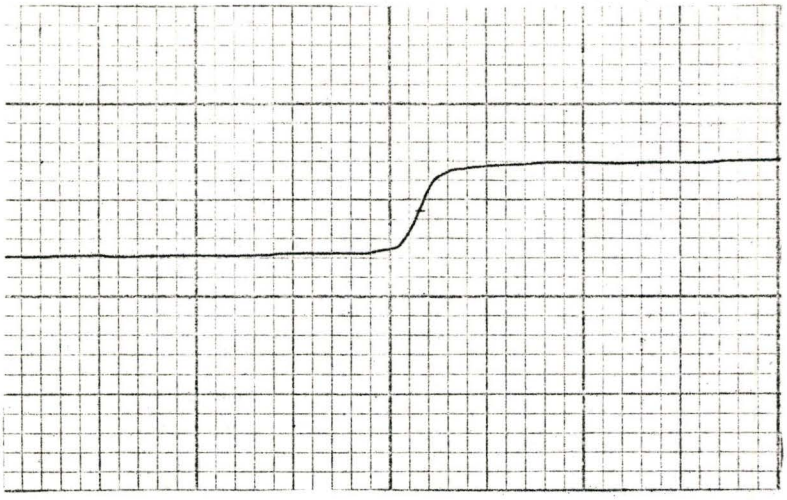

Fig. 2.6: Non-symmetric optical density scan for 0.5 cm thick lucite sample, exposed to standard neutron flux for 8 minutes.

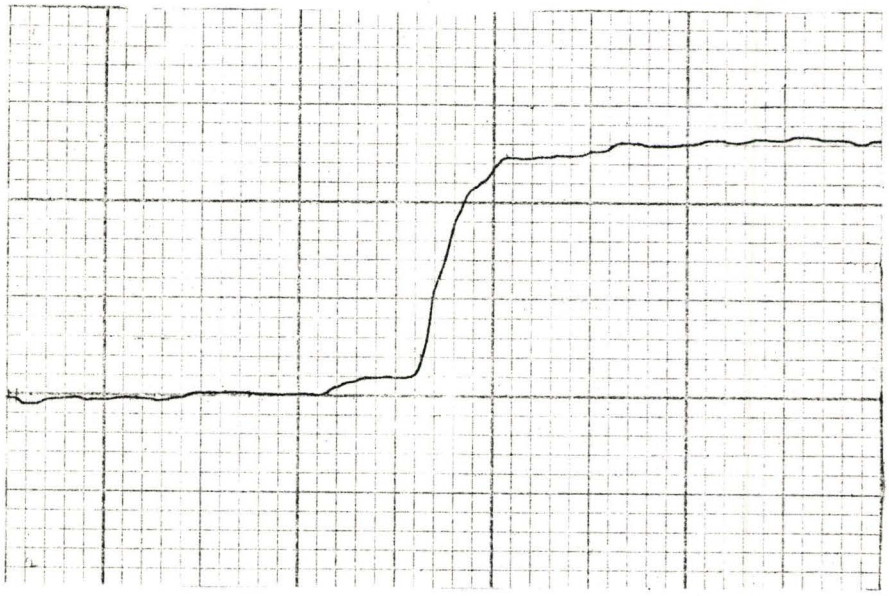

Fig. 2.7: Non-symmetric optican density scan for 0.7 cm thick lucite sample, exposed to standard neutron flux for 4 minutes.

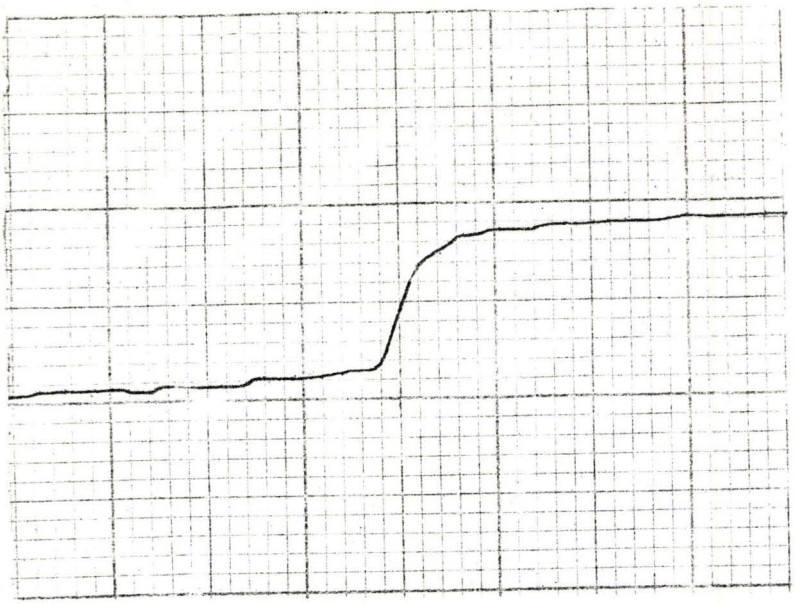

Fig. 2.8: Non-symmetric optical density scan for 0.7 cm thick lucite sample, exposed to standard neutron flux for 6 minutes.

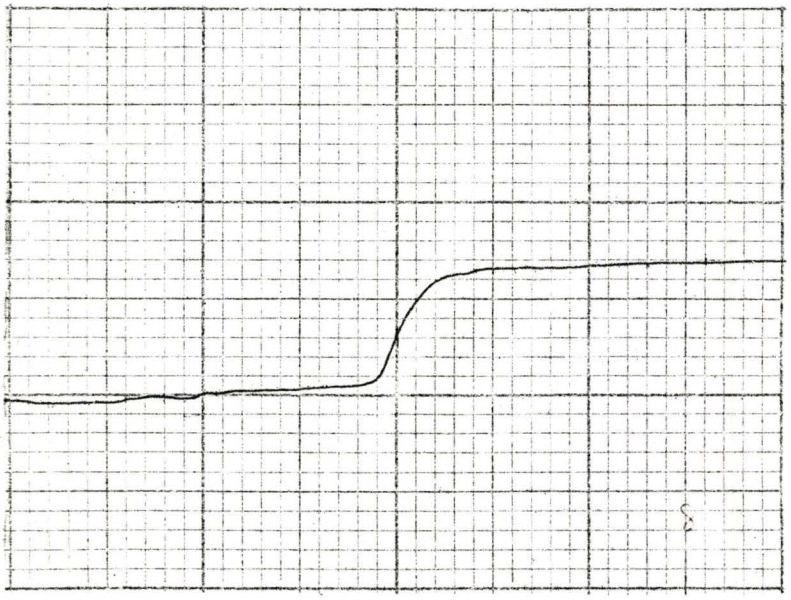

Fig. 2.9: Non-symmetric optical density scan for 0.7 cm thick lucite sample, exposed to standard neutron flux for 8 minutes.

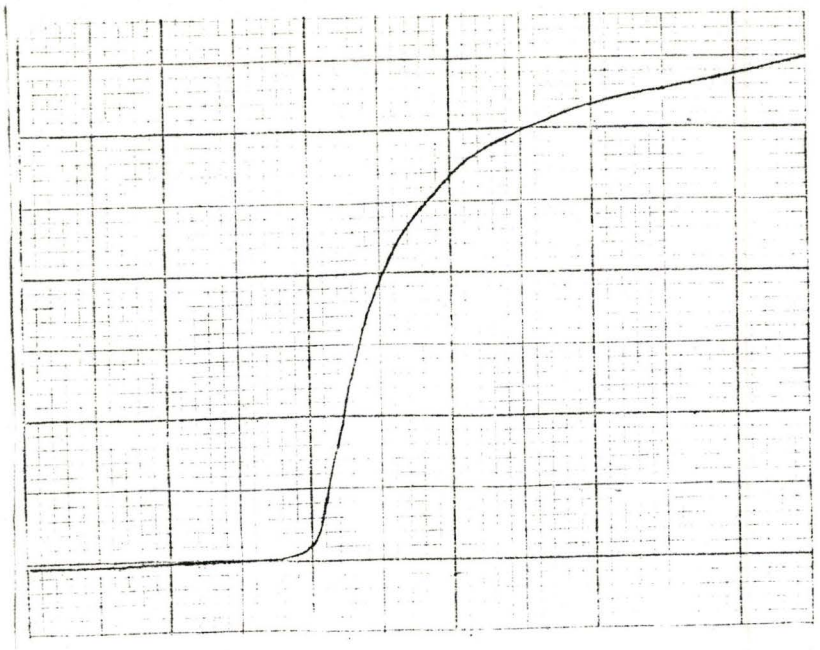

Fig. 2.10: Non-symmetric optical density scan for 1.0 cm thick lucite sample, exposed to standard neutron flux for 6 minutes.

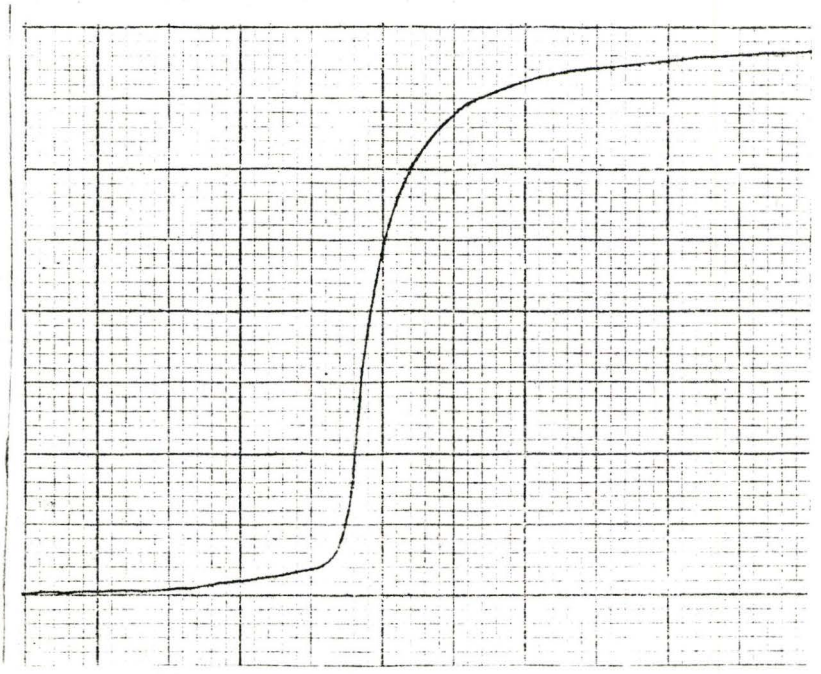

Fig. 2.11: Non-symmetric optical density scan for 1.2 cm thick lucite sample, exposed to standard neutron flux for 4 minutes.

Aside from the visual analysis, the non-symmetry of the ESF was further established by measuring the optical densities from the scans and feeding the data into a computer code which calculates the Lorentzian constant, C_L by using the symmetric form of the ESF. Results usually obtained when no scattering is involved are such that the values of C_L increase with increasing thickness of the knife edge for a given material[7]; but for the case of lucite, no such regular trend was obtained, which suggests that a new formulation is required to account for the scattering.

For illustrative comparative purpose we show in Fig. 2.12 the symmetric and non-symmetric optical densities.

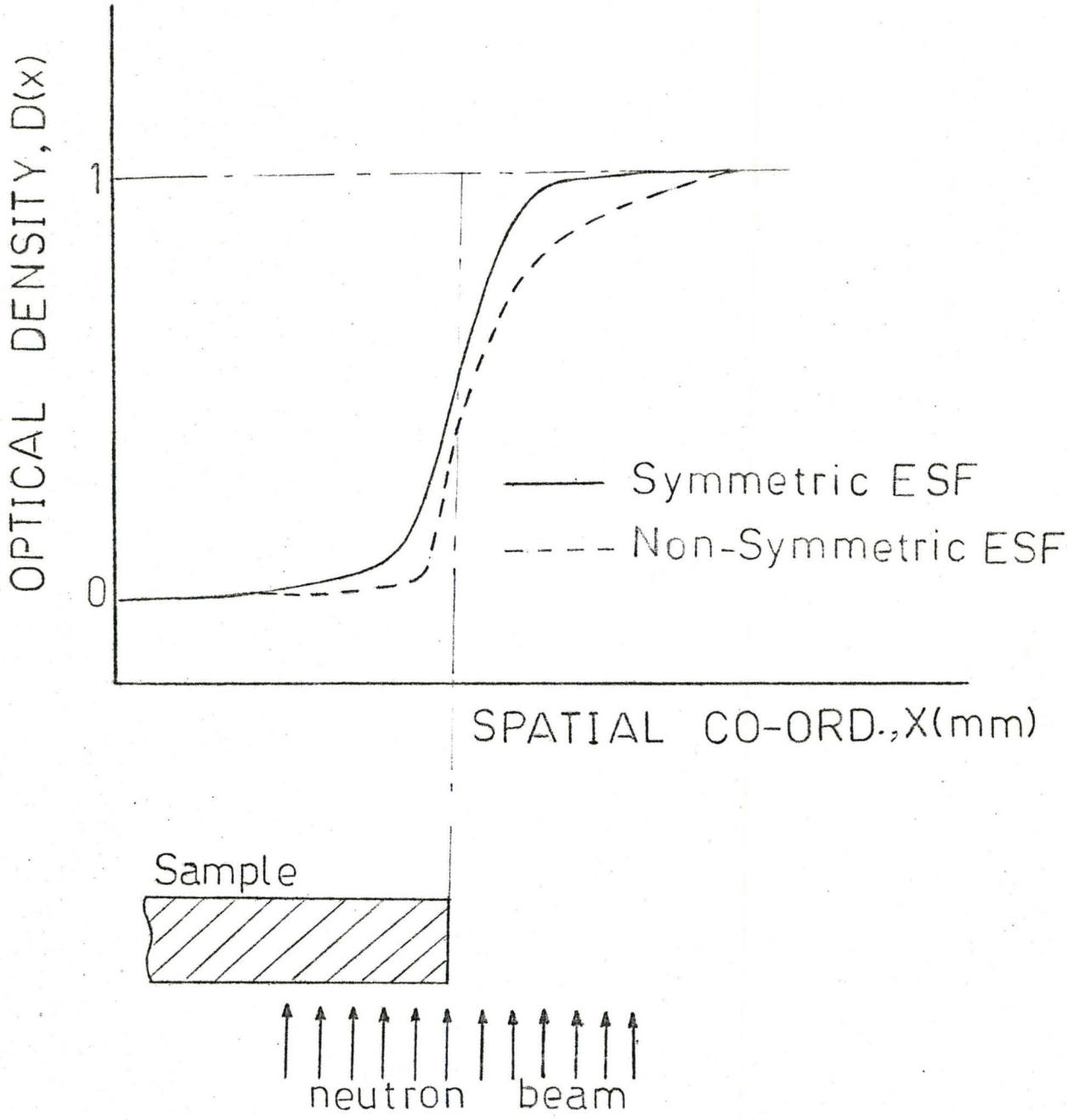

Fig. 2.12: Symmetric and non-symmetric forms of optical density.

CHAPTER 3

THEORETICAL ANALYSIS

3.1 Introduction

As mentioned in the Introduction, one basic assumption which has been made here is that any scattered neutron suffers only a single scattering before getting absorbed or leaving the sample. This assumption makes the analysis less complicated and relies on build up factors for any modifications to include multiple scattering. Two different models have been presented and the first model has been treated in both polar and Cartesian coordinates; the reader may find the Cartesian form a little easier to follow.

3.2.1 Model I: Single Scattering Approach - Polar

The theory is based on the probability that a neutron will, following an attenuated penetration into the specimen, undergo an isotropic scattering event. Figure 3.1 shows the general form which the model takes. The details are now described.

A neutron incident on the sample in the direction shown, travels attenuated to a point A, through a distance r_1 ($o \leq r \leq b$, where b is the thickness of the sample), and is then scattered isotropically. The scattered neutron now travels without further scattering through another distance, r_2 before leaving the sample. Once outside the sample, the neutron undergoes no further attenuation and continues in a free flight

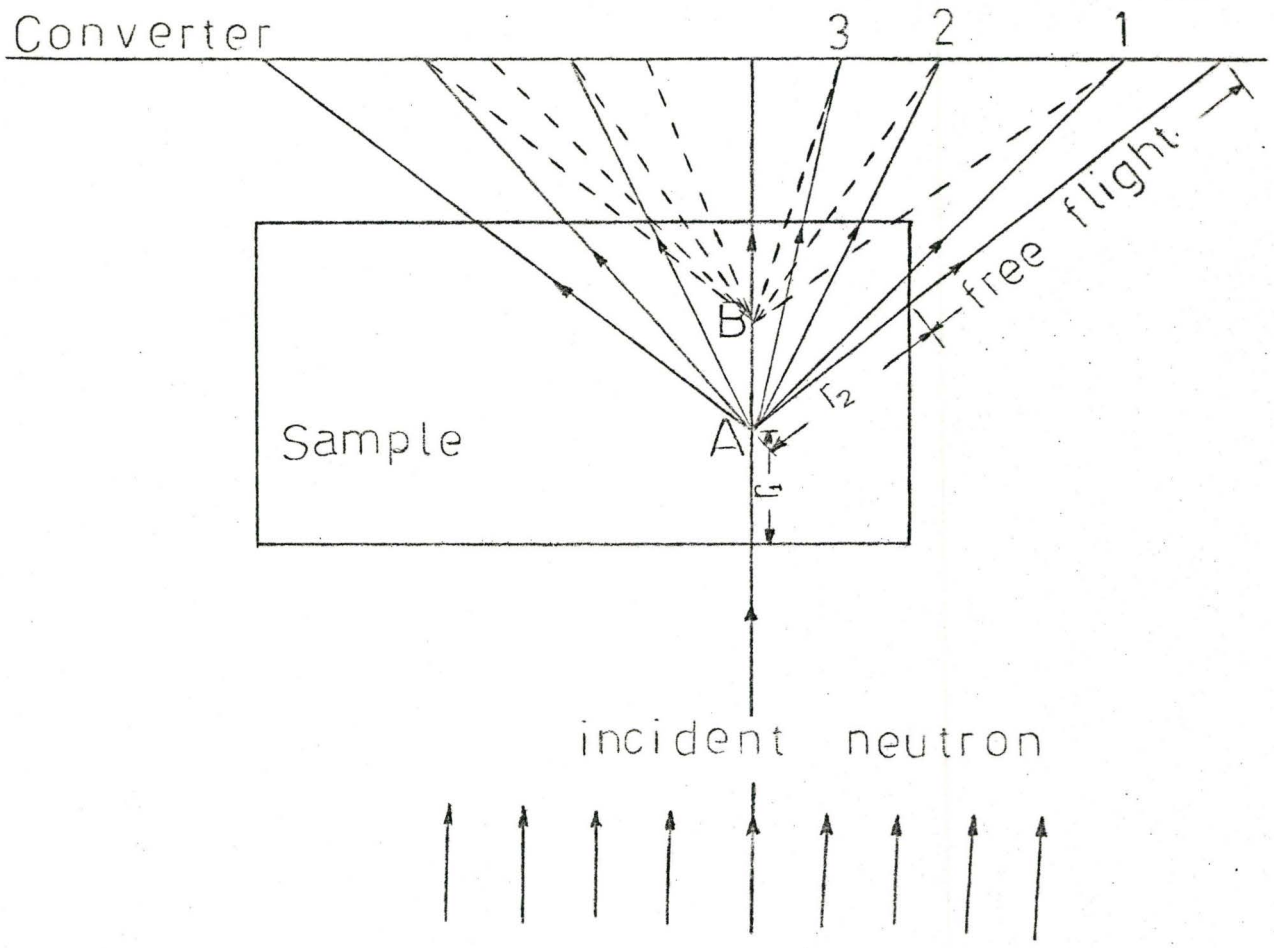

Fig. 3.1: The general form of the single scattering model illustrating how scattered neutrons can reach the converter.

until it reaches the converter. We shall not be concerned with what happens in the converter as this has been covered in many literatures[3], but we shall have to incorporate the knowledge available in this regard to our result in order to attain our goal.

As shown in Fig. 3.1, the neutrons scattered from point A have a chance of getting to any point on the converter, as are the neutrons scattered from point B. The flux reaching the point marked 1 on the converter from A is simply given by

$$\phi_o e^{-\Sigma r_1} e^{-\Sigma r_2} = \phi_o e^{-\Sigma(r_1 + r_2)} \tag{3.1}$$

where ϕ_o is the flux incident on the sample, and $\phi_o e^{-\Sigma r_1}$ is the fraction of this flux reaching the point A. Similarly, the flux reaching the same point 1 from B is given by the same expression but different values of r_1 and r_2; thus, the flux scattered from every point in the sample reaching each of the points 1,2,3, etc. on the converter.

We therefore require to obtain the total neutron flux reaching each point on the converter due to scattering from all the points in the sample. To do this, we shall make our model clearer by including all the necessary coordinates as shown in Fig. 3.2 and we shall, without any loss of generality, allow the converter to be in contact with the sample as this will help to simplify the geometry.

In Fig. 3.2, the coordinate u represents the points on the converter, and θ is the scattering angle of the neutrons which are initially travelling in the z-direction, while x denotes various points along the length of the sample. From the geometry of the figure we have

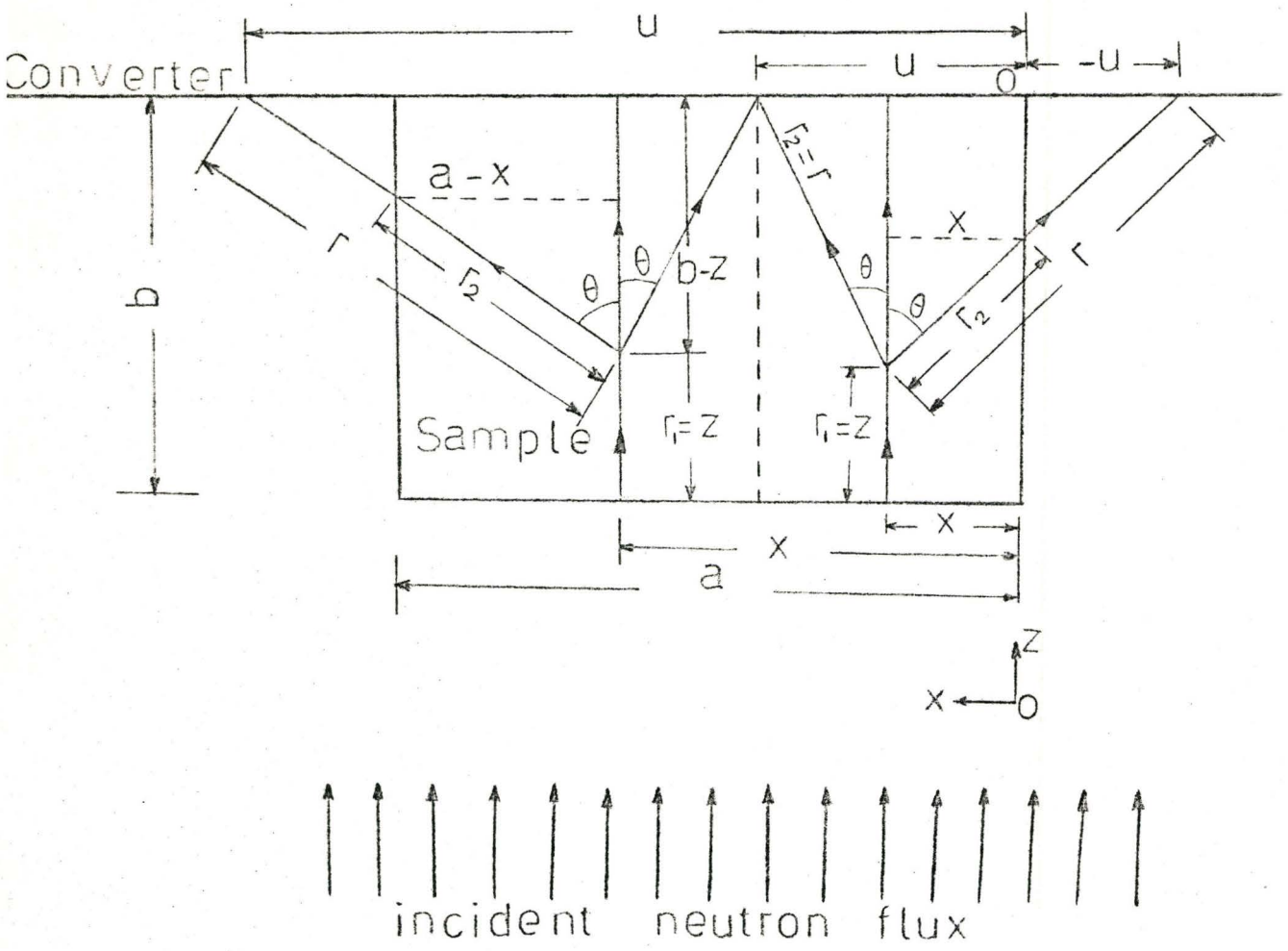

Fig. 3.2: The single scattering model in polar-coordinate representation.

$$r = \frac{b - z}{\cos \theta} = (b - z) \sec \theta \tag{3.2}$$

where $\theta = \tan^{-1} \frac{|x-u|}{b-z}$

$$r_1 = z$$

$$r_2 = \begin{cases} r \quad , & \text{for } o \leq u \leq a \\ \frac{x}{x-u} r \ , & \text{for } u < o \\ \left|\frac{a-x}{x-u}\right| r \ , & \text{for } u > a \end{cases} \tag{3.3}$$

Making use of Eq. (3.1), the scattered flux reaching any point u on the converter will be given by the general form

$$\phi_s(u) = \phi_o \iint e^{-\Sigma(r_1 + r_2)} \, dr_1 dr_2 \tag{3.4}$$

where the subscript, s, denotes scattering. Since the regions of the converter not directly behind the sample also have different flux ϕ_o, reaching them, we can represent the total flux, ϕ_T, at various points in different regions of the converter as

$$\begin{aligned} \phi_T(o \leq u \leq a) &= \phi_s(o \leq u \leq a) \\ \phi_T(u < o) &= \phi_o + \phi_s(u < a) \\ \phi_T(u > a) &= \phi_o + \phi_s(u > a) \end{aligned} \tag{3.5}$$

We now require to make substitutions for r_1 and r_2 in terms of θ and z, and also make the necessary transformations for change of variables in Eq. (3.4).

Since $\theta = \tan^{-1} \frac{|x-u|}{b-z}$

$z = b - |x-u| \cot \theta$

Hence $r_1 = z(\theta)$ (3.6)

also $r_2 = r_2(\theta,z)$ (3.7)

and, if we allow the incident flux ϕ_o to represent a unit flux, the scattered flux takes the form

$$\phi_s(u) = \iint f(r_1,r_2)dr_1dr_2 = \iint e^{-\Sigma(r_1 + r_2)}dr_1dr_2$$
$$= \iint f(\theta,z)J(\frac{r_1,r_2}{\theta,z})\, d\theta dz \tag{3.8}$$

where the Jacobian of transformation is

$$J(\frac{r_1,r_2}{\theta,z}) = \left|\frac{\partial(r_1,r_2)}{\partial(\theta,z)}\right| \tag{3.9}$$

and the Functional Determinant

$$\frac{\partial(r_1,r_2)}{\partial(\theta,z)} = \begin{vmatrix} \frac{\partial r_1}{\partial \theta} & \frac{\partial r_2}{\partial \theta} \\ \frac{\partial r_1}{\partial z} & \frac{\partial r_2}{\partial z} \end{vmatrix} \tag{3.10}$$

From Eq. (3.2) and Eq. (3.3) we know r_1 and r_2 in terms of θ and z and we shall evaluate the Jacobian only in one region of the converter, since the values in the other regions will only differ by a multiplication factor.

In the region $o \leq u \leq a$ we have

$$\frac{\partial(r_i,r_2)}{\partial(\theta,z)} = \begin{vmatrix} |x-u|\ \csc^2\theta & (b-z)\sec\theta\ \tan\theta \\ 1 & -\sec\theta \end{vmatrix} \tag{3.11}$$

and the Jacobian of transformation is given by

$$J(\frac{r_1,r_2}{\theta,z}) = \begin{cases} (b-z)\sec\theta\ \tan\theta + |x-u|\csc^2\theta\ \sec\theta\ , & 0 \leq u \leq a \\ \frac{x}{x-u}\ \{(b-z)\sec\theta\ \tan\theta + |x-u|\csc^2\theta\ \sec\theta\}\ , & u < o \\ \frac{a-x}{x-u}\ \{(b-z)\sec\theta\ \tan\theta\ + |x-u|\csc^2\theta\sec\theta\}\ , & u > a \end{cases} \tag{3.12}$$

Making the substitutions we have

$$\phi_s(o \leq u \leq a) = \int \int^{\theta} e^{-\Sigma[z + (b-z)\sec\theta]}\ \{(b-z)\sec\theta\tan\theta + |x-u|\sec\theta\ \csc^2\theta\}\ d\theta dz \tag{3.13}$$

$$\phi_s(u < o) = \int \int e^{-\Sigma[z + (b-z)\ \frac{u}{x-u}\ \sec\theta]}\ \frac{x}{x-u}\ \{(b-z)\sec\theta\ \tan\theta + |x-u|\sec\theta\ \csc^2\theta\}d\theta dz \tag{3.14}$$

$$\phi_s(u > a) = \int \int e^{-\Sigma[z + (b-z)\frac{a-x}{|x-l|}\sec\theta]} \frac{a-x}{|x-u|}\{(b-z)\sec\theta\tan\theta + |x-u|\sec\theta\csc^2\theta\}d\theta dz \tag{3.15}$$

where

$$z_1 = 0$$

$$z_2 = b \tag{3.16}$$

$$\theta_1 = \tan^{-1}\frac{|u|}{b-z}$$

and

$$\theta_2 = \tan^{-1}\frac{|a-u|}{b-z}$$

Equations (3.13), (3.14) and (3.15) give the required expressions for the scattered flux in the polar coordinate representation. It is now a matter of numerical computation to obtain the values at each point on the converter. A computer program required to handle this double integration must take care of all cases for which the integrand can blow up as a result of the angle θ assuming certain values; and this could happen

quite easily due to the different forms of trigonometrical functions involved. It could also happen when u and x assume the same values.

Some of these flaws are greatly reduced in the Cartesian coordinate representation because in place of the trigonometrical functions, square roots of squared quantities are involved; the squaring takes care of any negative quantities.

3.2.2 Model I: Single Scattering Approach - Cartesian

The theory is essentially the same as in the polar coordinate representation, and we shall continue to denote the coordinate of the points on the converter with u. The distances r_1 and r_2 through which the neutron travels will now be given in terms of x and y only as suggested by Fig. 3.3.

In this case, we can define a common distance r from any point on the converter by the relation:

$$r = \sqrt{(x-u)^2 + (1-y)^2} \tag{3.17}$$

and the distances through which the neutrons are scattered in the sample before reaching various regions of the converter are then given by

$$r_2 = \frac{u}{x-u} . r \quad ; \; u \leq o \tag{3.18a}$$

$$r_2 = r \quad ; \; o \leq u \leq a \tag{3.18b}$$

$$r_2 = \frac{a-x}{u-x} . r \quad ; \; u > a \tag{3.18c}$$

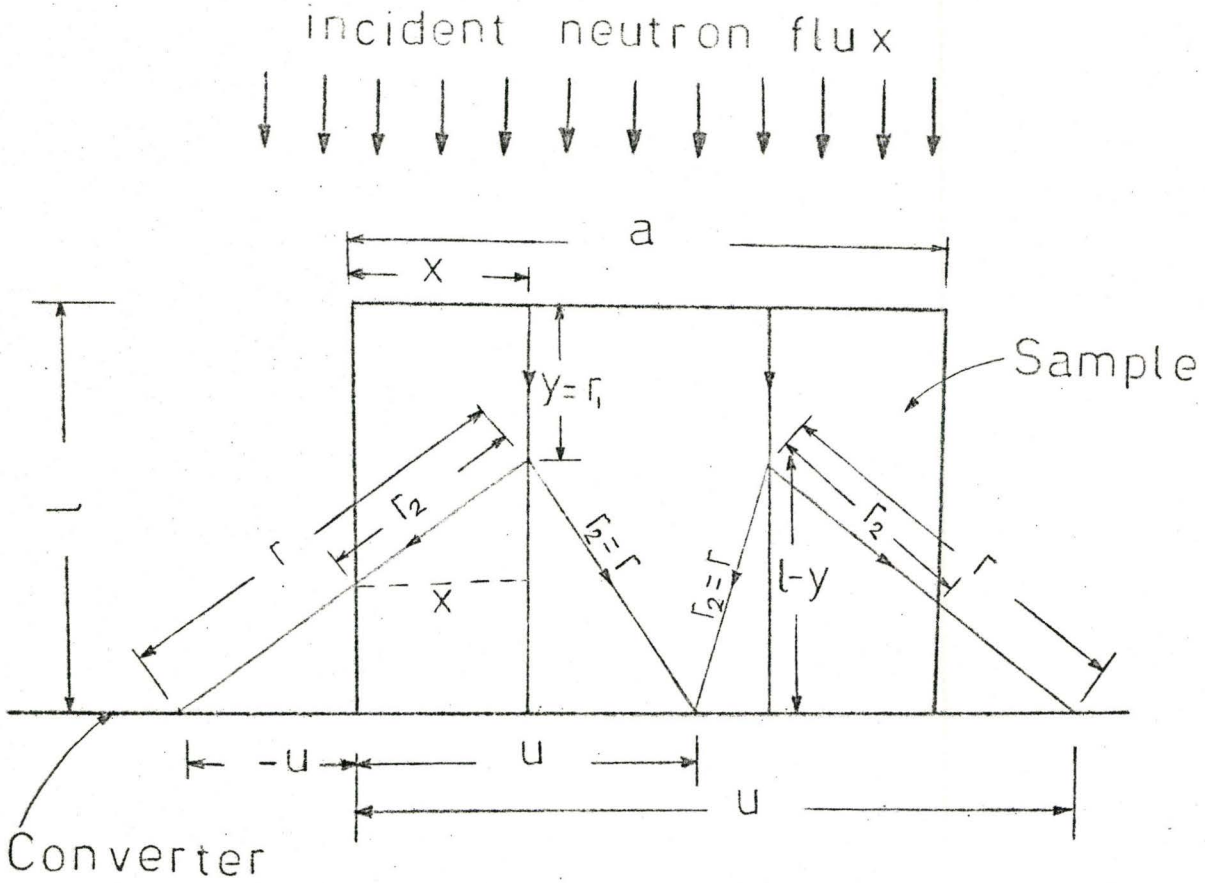

Fig. 3.3: The single scattering model in Cartesian-coordinate representation.

The scattered flux now takes the form

$$\phi_s(u) = \iint f(x,y)\ J\left(\frac{r_1,r_2}{x,y}\right)dxdy \tag{3.19}$$

We shall proceed directly to obtain the Jacobian of transformation for the various regions of the converter.

In all cases, the distance which the neutron travels attenuated in the sample before scattering is given by $r_1 = y$ ($o \leq y \leq l$, where l is the thickness of the sample).

For $r_1 = y$

$$\frac{\partial r_1}{\partial y} = 1; \quad \frac{\partial r_1}{\partial x} = 0 \tag{3.20}$$

and for $u \leq o$ we have

$$r_2 = \frac{x}{x-u}\ \sqrt{(x-u)^2 + (\ell-y)^2} \tag{3.21a}$$

$$\frac{\partial r_2}{\partial x} = \frac{x}{\{(x-u)^2 + (\ell-y)^2\}^{1/2}} - \frac{u}{(x-u)^2}\ \{(x-u)^2 + (\ell-y)^2\}^{1/2} \tag{3.21b}$$

$$\frac{\partial r_2}{\partial y} = \frac{-x(\ell-y)}{(x-u)\{(x-u)^2 + (\ell-y)^2\}^{1/2}} \tag{3.21c}$$

With the Jacobian of transformation given by

$$J\left(\frac{r_1,r_2}{x,y}\right) = \left|\frac{\partial(r_1,r_2)}{\partial(x,y)}\right| \tag{3.22}$$

where

$$\frac{\partial(r_1,r_2)}{\partial(x,y)} = \begin{vmatrix} \frac{\partial r_1}{\partial x} & \frac{\partial r_2}{\partial x} \\ \frac{\partial r_1}{\partial y} & \frac{\partial r_2}{\partial y} \end{vmatrix} \tag{3.23}$$

we have

$$J(u \leq o) = \left| \frac{x}{\{(x-u)^2 + (\ell-y)^2\}^{1/2}} - \frac{u}{x-u}\{1 + (\frac{\ell-y}{x-u})^2\}^{1/2} \right| \tag{3.24}$$

For $o \leq u \leq a$ we have

$$r_2 = \{(x-u)^2 + (\ell-y)^2\}^{1/2} \tag{3.25a}$$

$$\frac{\partial r_2}{\partial x} = (x-u)\{(x-u)^2 + (\ell-y)^2\}^{1/2} \tag{3.25b}$$

$$\frac{\partial r_2}{\partial y} = -(\ell-y)\{(x-u)^2 + (\ell-y)^2\}^{-1/2} \tag{3.25c}$$

and

$$J(o \leq u \leq a) = \left| \frac{x-u}{\{(x-u)^2 + (\ell-y)^2\}^{1/2}} \right| \tag{3.26}$$

$$= \frac{1}{\sqrt{1 + (\frac{\ell-y}{x-u})^2}}$$

For $u \geq a$ we have

$$r_2 = \frac{a-x}{u-x} \sqrt{(u-x)^2 + (\ell-y)^2} \tag{3.27a}$$

$$\frac{\partial r_2}{\partial x} = \frac{(a-x)}{\{(u-x)^2 + (\ell-y)^2\}^{1/2}} - \frac{u-a}{u-x}\{1 + (\frac{\ell-y}{u-x})^2\}^{1/2} \tag{3.27b}$$

$$\frac{\partial r_2}{\partial y} = \frac{-(a-x)(\ell-y)}{(u-x)\{(u-x)^2 + (\ell-y)^2\}^{1/2}} \tag{3.27c}$$

and

$$J(u \geq a) = \left| \frac{(a-x)}{\{(u-x)^2 + (\ell-y)^2\}^{1/2}} - \frac{(u-a)}{(u-x)}\{1 + (\frac{\ell-y}{u-x})^2\}^{1/2} \right| \tag{3.28}$$

The validity of these transformation functions can easily be varified by noting that the following boundary conditions are satisfied:

$$J(u \geq a)\Big|_{u=a} = J(o \leq u \leq a)\Big|_{u=a} \tag{3.29}$$

and

$$J(o \leq u \leq a)\Big|_{u=o} = J(u \leq o)\Big|_{u=0} \tag{3.30}$$

The form which the scattered flux assumes in the various regions of the converter can now be given in the Cartesian representation by the following relations

$$\phi_s(u \leq o) = \int_o^{\ell}\int_o^{a} e^{-\Sigma\{y + \frac{x}{x-u}\sqrt{(x-u)^2 + (\ell-y)^2}\}} * J(u \leq o)\,dx\,dy \tag{3.31}$$

$$\phi_s(o \leq u \leq a) = \int_o^{\ell}\int_o^{a} e^{-\Sigma\{y + \sqrt{(x-u)^2 + (\ell-y)^2}\}} * J(o \leq u \leq a)\,dx\,dy \tag{3.32}$$

$$\phi_s(u \geq a) = \int_0^{\ell}\int_0^{a} e^{-\Sigma\{y + \frac{a-x}{u-x}\sqrt{(u-x)^2 + (\ell-y)^2}\}} * J(u \geq a)dxdy \qquad (3.33)$$

where the J's are as obtained in Eqs. (3.24), (3.26) and (3.28).

With the scattered flux now given by Eqs. (3.31), (3.32) and (3.33) and the total flux defined by Eq. (3.5), the non-symmetric edge spread function, $S_N(u,x)$ takes the form

$$S_N(u,x) = \int_{u_1}^{u_2} \phi_T(u)L(u,x)du \qquad (3.34)$$

$$= \int_{u_1}^{u_2} \frac{\phi_T(u)du}{1 + C(x-u)^2} \qquad (3.35)$$

3.3 Model II: Shielding Concept Approach

Another approach to the problem of accounting for the non-symmetric edge spread function can be provided by considering the sample to consist of tinny strips alligned parallel to the direction of the incident neutron flux; we can then focus attention on each of the strips, with each point on the strip acting as a neutron source, while the rest of the sample acts as a shielding medium.

To obtain the total flux reaching each point on the converter, we shall sum the flux from each point source over all the point sources per strip, and then sum over all the strips in the sample keeping in mind that our point source emitts neutrons isotropically. The geometry for this model is essentially the same as with the single scattering model, but with the sample now consisting of strips, Fig. 3.4

Our first task is obtaining the source strength of each point on the strip. As the incident neutrons make their entrants into the sample,

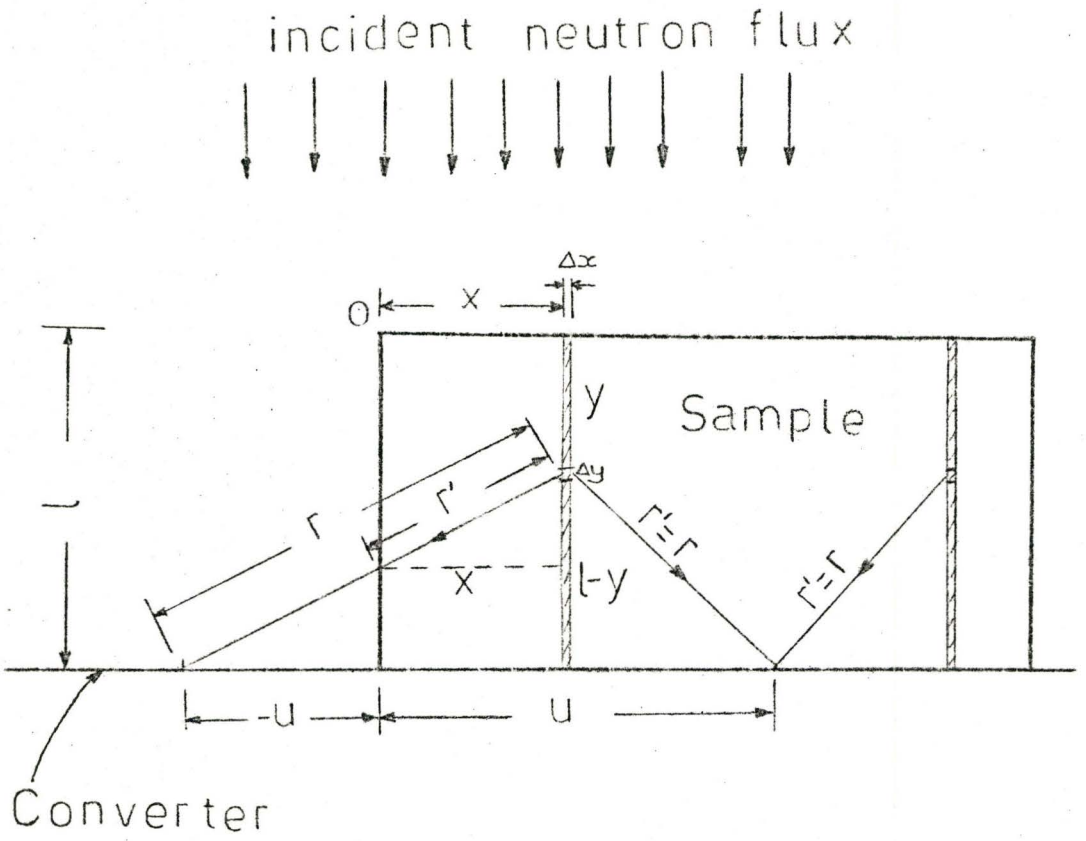

Fig. 3.4: The shielding model.

they immediately begin to suffer attenuation along each strip. The source strength at each point will then be given by $\phi_o e^{-\Sigma t y}$, where y is the distance travelled by the neutron along the strip up to the point being considered, Σ_t is the total cross-section of the sample material, and ϕ_o is the incident neutron flux.

From the geometry of the model shown in Fig. 3.4, the distance r between each point source and the points u, on the converter, is given by

$$r = \sqrt{(x-u)^2 + (\ell-y)^2} \tag{3.36}$$

the distance r' for which the neutrons from the point source are further attenuated before reaching the converter is given by

$$r' = r \quad , u > o \tag{3.37a}$$

$$r' = \frac{x}{x-u}.r \quad , u < o \tag{3.37b}$$

If we now denote the flux from each point on the strip to the converter by $R_{pt}(y,r')$, we have

$$R_{pt}(y,r') = \frac{1}{4\pi} \phi_o \, e^{-\Sigma t y} \, e^{-\Sigma t r'} \tag{3.38}$$

the factor 1/4 π is the fraction of the flux in any direction from the isotropic point source.

The total flux $R_{ln}(y,r')$ from the strip is then given by

$$R_{\ell n}(y,r') = \sum_{n=1}^{N} R_{pt}\,\Delta y \tag{3.39}$$

where Δy is the step length along the strip.

The overall total flux $R_u(y,r')$ at a point u, from all the strips in the sample will then be given by

$$\begin{aligned} R_u(y,r') &= \sum_{s=1}^{N} R_{\ell n}\,\Delta x \\ &= \sum_{s=1}^{S} \left(\sum_{n=1}^{N} R_{pt}\,\Delta y \right) \Delta x \end{aligned} \tag{3.40}$$

where Δx is the thickness of each small strip.

Substituting for $R_{pt}(y,r')$ we finally have

$$R_u(y,r') = \frac{\phi_o}{4\pi} \sum_{s=1}^{S} \sum_{n=1}^{N} e^{-\Sigma t(y+r')}\,\Delta y \Delta x \tag{3.41}$$

CHAPTER 4

NUMERICAL INVESTIGATION

4.1 Programming

The computation of the flux given by Eqs (3.31), (3.32) and (3.33) was carried out numerically by incorporating a number of library programs into the main program as shown in the Appendix. The first of these library routines, DCS2QU computes the approximate double integral to a given set of data using a natural bicubic spline interpolate; and in our case, the set of data are values of the integrand calculated at various mesh points by a computer simulation of the sample model. The value of the integral from DCS2QU corresponds to the scattered flux, $\phi_S(u)$ reaching the point u.

Two other library routines, ISCICU and DSCQDU were used to obtain the form of the non-symmetric edge spread function, $S_N(u,x)$, by integrating the total flux, $\phi_T(u)$, at u, Eq. (3.5), with the Lorentzian function, $L(u,x)$:

$$S_N(u,x) = N \int_{-\infty}^{u} \frac{\phi_T(u)du}{1 + C_L(x-u)^2} \tag{4.1}$$

In Eq. (4.1) x is the coordinate on the film in the back converter system. The Lorentzian constant, C_L, which is a function of the radiographic system, and hence depends on the material of the sample has not been previously measured for lucite. This quantity C_L is thus treated as a free parameter in the computation of the non symmetric edge spread function, but with the values chosen within the ranges of known

values of C_L.

4.2 Result of Numerical Investigation

The results of the numerical investigations presented in this section are the data and graphic output obtained directly from the computer code NEUT77, for the single scattering model.

A remarkable observation about the flux shape, is that it takes a form similar to the non symmetric edge spread function or the optical density across the sample edge; this is consistent with the direct proportionality of the flux with the optical density in the linear response range of the film. The flux in the region of the sample, shows some numerical instability and this tends to smoothen out with a more refined integration mesh. The flux in this region also show some distinct variation as the sample thickness was varied. Fig. 4.1(a), 4.2(a) and 4.3(a) show these flux shapes for various thicknesses of the sample.

The results of integrating each of the above flux with the Lorentzian function gave results shown in Fig. 4.1(b), 4.2(b) and 4.3(b) which are quite comparable with the experimental results of Fig. 2.3(a), (b) and 2.4(a),(b).

Table I: COMPUTER OUTPUT OF THE TOTAL FLUX, $\phi(U)$ REACHING EACH POINT U ON THE CONVERTER

U(cm)	$\phi(U)$	U(cm)	$\phi(U)$
-.51000E+00	.19934E+01	0.	.19925E+01
-.50000E+00	.20116E+01	.10000E-01	.20034E+01
-.49000E+00	.19932E+01	.20000E-01	.20083E+01
-.48000E+00	.19933E+01	.30000E-01	.21118E+01
-.47000E+00	.19934E+01	.40000E-01	.21147E+01
-.46000E+00	.19934E+01	.50000E-01	.21173E+01
-.45000E+00	.19934E+01	.60000E-01	.21185E+01
-.44000E+00	.19933E+01	.70000E-01	.22135E+01
-.43000E+00	.19932E+01	.80000E-01	.22235E+01
-.42000E+00	.19930E+01	.90000E-01	.22335E+01
-.41000E+00	.19928E+01	.10000E+00	.22435E+01
-.40000E+00	.19926E+01	.11000E+00	.22535E+01
-.39000E+00	.19923E+01	.12000E+00	.22635E+01
-.38000E+00	.19920E+01	.13000E+00	.22735E+01
-.37000E+00	.19916E+01	.14000E+00	.22835E+01
-.36000E+00	.19911E+01	.15000E+00	.22935E+01
-.35000E+00	.19906E+01	.16000E+00	.23035E+01
-.34000E+00	.19901E+01	.17000E+00	.23135E+01
-.33000E+00	.19895E+01	.18000E+00	.23235E+01
-.32000E+00	.19888E+01	.19000E+00	.23335E+01
-.31000E+00	.19880E+01	.20000E+00	.23435E+01
-.30000E+00	.19872E+01	.21000E+00	.23535E+01
-.29000E+00	.19863E+01	.22000E+00	.23635E+01
-.28000E+00	.19853E+01	.23000E+00	.23735E+01
-.27000E+00	.19843E+01	.24000E+00	.23835E+01
-.26000E+00	.19832E+01	.25000E+00	.23935E+01
-.25000E+00	.19820E+01	.26000E+00	.24035E+01
-.24000E+00	.19807E+01	.27000E+00	.24135E+01
-.23000E+00	.19793E+01	.28000E+00	.24235E+01
-.22000E+00	.19778E+01	.29000E+00	.24335E+01
-.21000E+00	.19762E+01	.30000E+00	.24435E+01
-.20000E+00	.19745E+01	.31000E+00	.24535E+01
-.19000E+00	.19727E+01	.32000E+00	.24635E+01
-.18000E+00	.19708E+01	.33000E+00	.24735E+01
-.17000E+00	.19687E+01	.34000E+00	.24835E+01
-.16000E+00	.19665E+01	.35000E+00	.24935E+01
-.15000E+00	.19642E+01	.36000E+00	.25035E+01
-.14000E+00	.19617E+01	.37000E+00	.25135E+01
-.13000E+00	.19591E+01	.38000E+00	.25235E+01
-.12000E+00	.19563E+01	.39000E+00	.25335E+01
-.11000E+00	.19534E+01	.40000E+00	.25435E+01
-.10000E+00	.19503E+01	.41000E+00	.25535E+01
-.90000E-01	.19471E+01	.42000E+00	.25635E+01
-.80000E-01	.19437E+01	.43000E+00	.25735E+01
-.70000E-01	.19401E+01	.44000E+00	.25835E+01
-.60000E-01	.19363E+01	.45000E+00	.25935E+01
-.50000E-01	.19322E+01	.46000E+00	.26035E+01
-.40000E-01	.19279E+01	.47000E+00	.26135E+01
-.30000E-01	.19233E+01	.48000E+00	.26235E+01
-.20000E-01	.19184E+01	.49000E+00	.26335E+01
-.10000E-01	.19132E+01		

Table II: COMPUTER OUTPUT OF THE OPTICAL DENSITY D(x), OBTAINED FOR 1.2 cm THICK LUCITE SAMPLE

X(cm)	D(x)
-.51000E+00	.6144E-01
-.50000E+00	.6137E-01
-.49000E+00	.6144E-01
-.48000E+00	.6120E-01
-.47000E+00	.6113E-01
-.46000E+00	.6109E-01
-.45000E+00	.6107E-01
-.44000E+00	.6107E-01
-.43000E+00	.6107E-01
-.42000E+00	.6099E-01
-.41000E+00	.6095E-01
-.40000E+00	.6093E-01
-.39000E+00	.6093E-01
-.38000E+00	.6098E-01
-.37000E+00	.6102E-01
-.36000E+00	.6104E-01
-.35000E+00	.6106E-01
-.34000E+00	.6107E-01
-.33000E+00	.6107E-01
-.32000E+00	.6107E-01
-.31000E+00	.6107E-01
-.30000E+00	.6108E-01
-.29000E+00	.6113E-01
-.28000E+00	.6119E-01
-.27000E+00	.6125E-01
-.26000E+00	.6131E-01
-.25000E+00	.6136E-01
-.24000E+00	.6141E-01
-.23000E+00	.6145E-01
-.22000E+00	.6149E-01
-.21000E+00	.6154E-01
-.20000E+00	.6161E-01
-.19000E+00	.6172E-01
-.18000E+00	.6185E-01
-.17000E+00	.6199E-01
-.16000E+00	.6221E-01
-.15000E+00	.6228E-01
-.14000E+00	.6243E-01
-.13000E+00	.6258E-01
-.12000E+00	.6274E-01
-.11000E+00	.6290E-01
-.10000E+00	.6309E-01
-.90000E-01	.6332E-01
-.80000E-01	.6358E-01
-.70000E-01	.6389E-01
-.60000E-01	.6428E-01
-.50000E-01	.6478E-01
-.40000E-01	.6549E-01
-.30000E-01	.6663E-01
-.20000E-01	.6880E-01
-.10000E-01	.7404E-01

X(cm)	D(x)
0.	.8449E-01
.10000E-01	.9036E-01
.20000E-01	.9332E-01
.30000E-01	.9524E-01
.40000E-01	.9665E-01
.50000E-01	.9778E-01
.60000E-01	.9871E-01
.70000E-01	.9951E-01
.80000E-01	.1002E+00
.90000E-01	.1008E+00
.10000E+00	.1013E+00
.11000E+00	.1018E+00
.12000E+00	.1023E+00
.13000E+00	.1027E+00
.14000E+00	.1031E+00
.15000E+00	.1033E+00
.16000E+00	.1036E+00
.17000E+00	.1039E+00
.18000E+00	.1041E+00
.19000E+00	.1044E+00
.20000E+00	.1046E+00
.21000E+00	.1048E+00
.22000E+00	.1050E+00
.23000E+00	.1052E+00
.24000E+00	.1053E+00
.25000E+00	.1055E+00
.26000E+00	.1056E+00
.27000E+00	.1058E+00
.28000E+00	.1059E+00
.29000E+00	.1060E+00
.30000E+00	.1061E+00
.31000E+00	.1062E+00
.32000E+00	.1063E+00
.33000E+00	.1064E+00
.34000E+00	.1065E+00
.35000E+00	.1066E+00
.36000E+00	.1067E+00
.37000E+00	.1068E+00
.38000E+00	.1069E+00
.39000E+00	.1069E+00
.40000E+00	.1070E+00
.41000E+00	.1071E+00
.42000E+00	.1071E+00
.43000E+00	.1072E+00
.44000E+00	.1072E+00
.45000E+00	.1073E+00
.46000E+00	.1073E+00
.47000E+00	.1074E+00
.48000E+00	.1074E+00
.49000E+00	.1075E+00

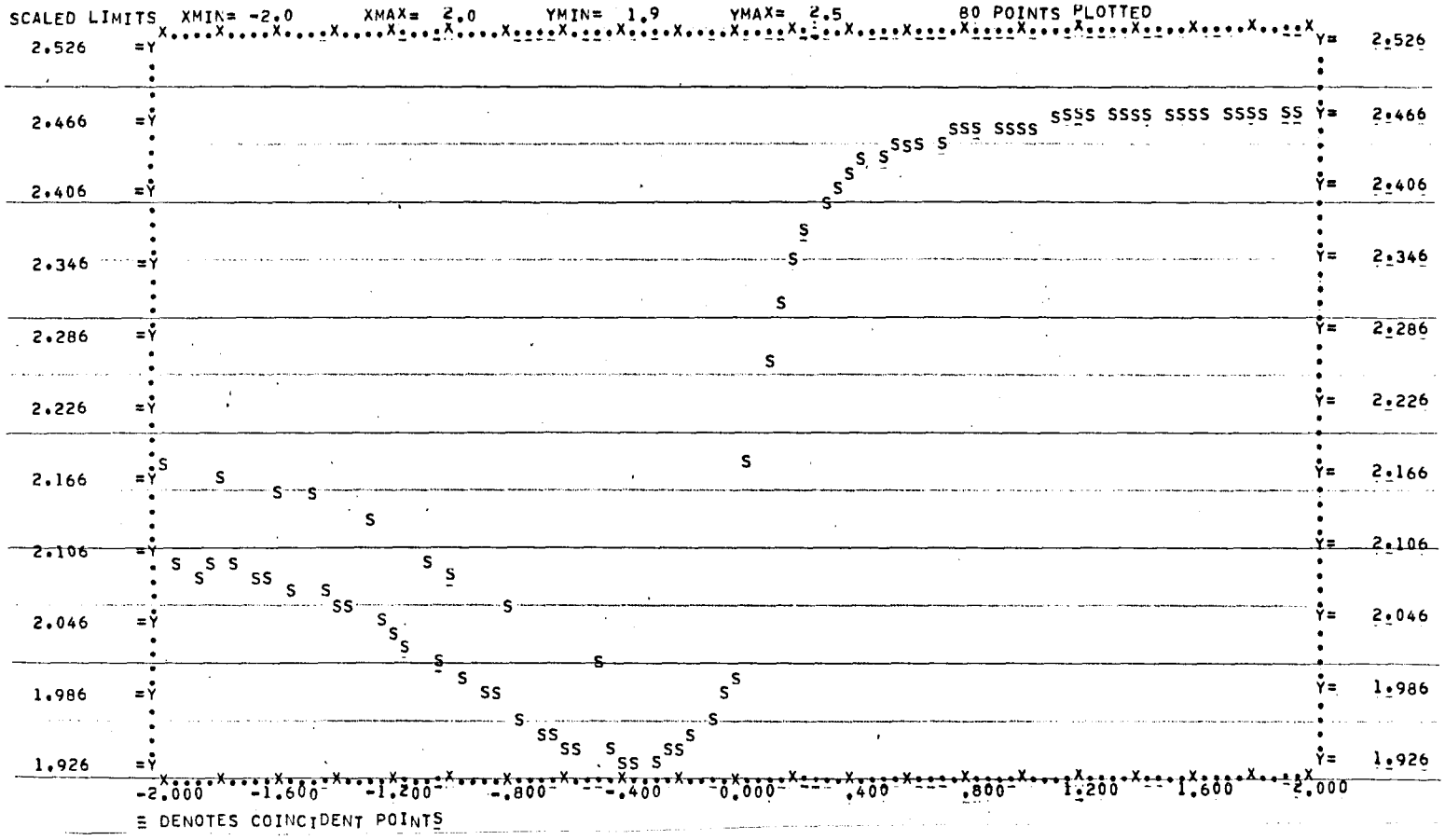

Fig. 4.1(a): Graphic computer output of the flux shape for 1.0 cm thick lucite sample, using the single scattering model.

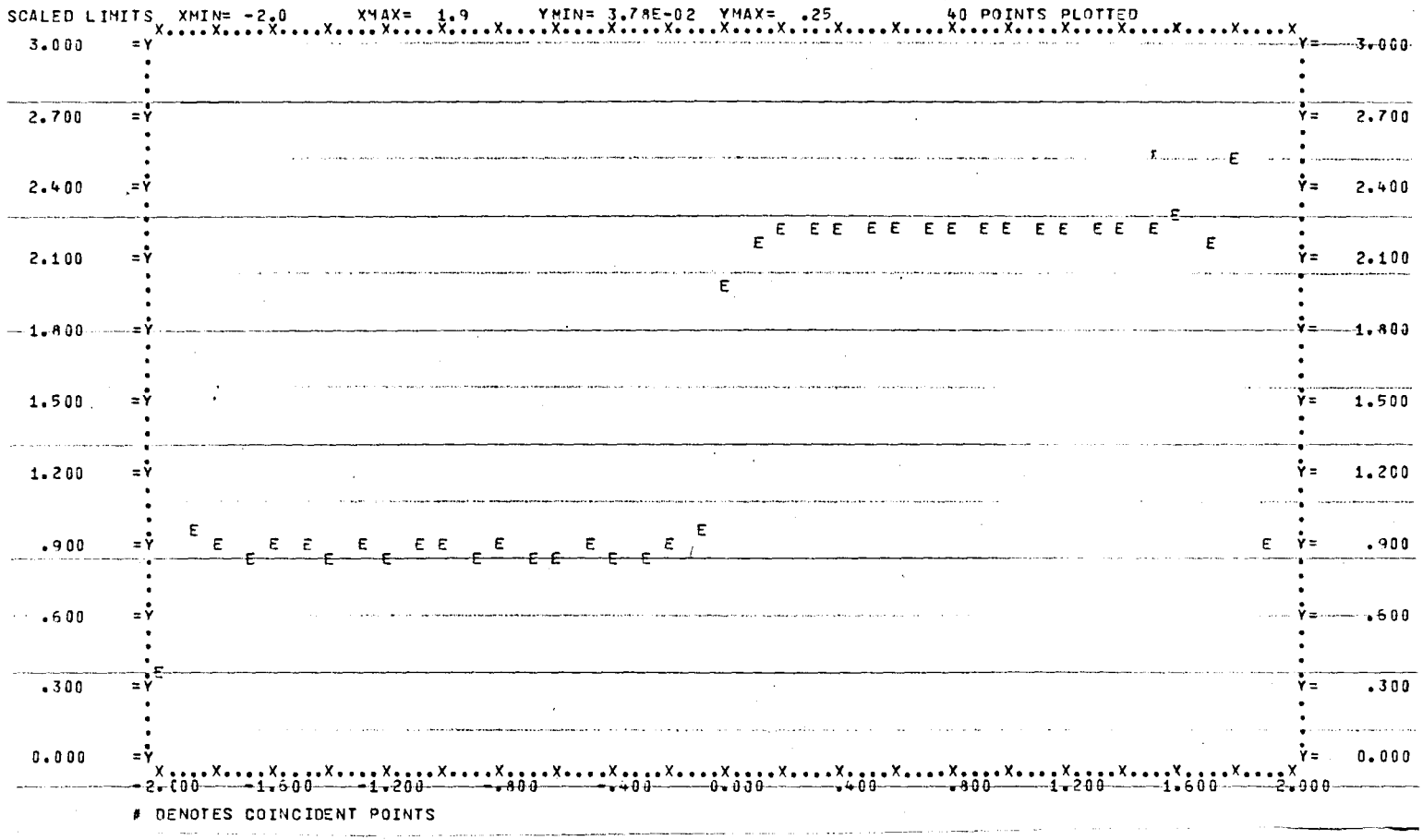

Fig. 4.1(b): Graphic computer output of the flux shape for 1.0 cm thick lucite sample.

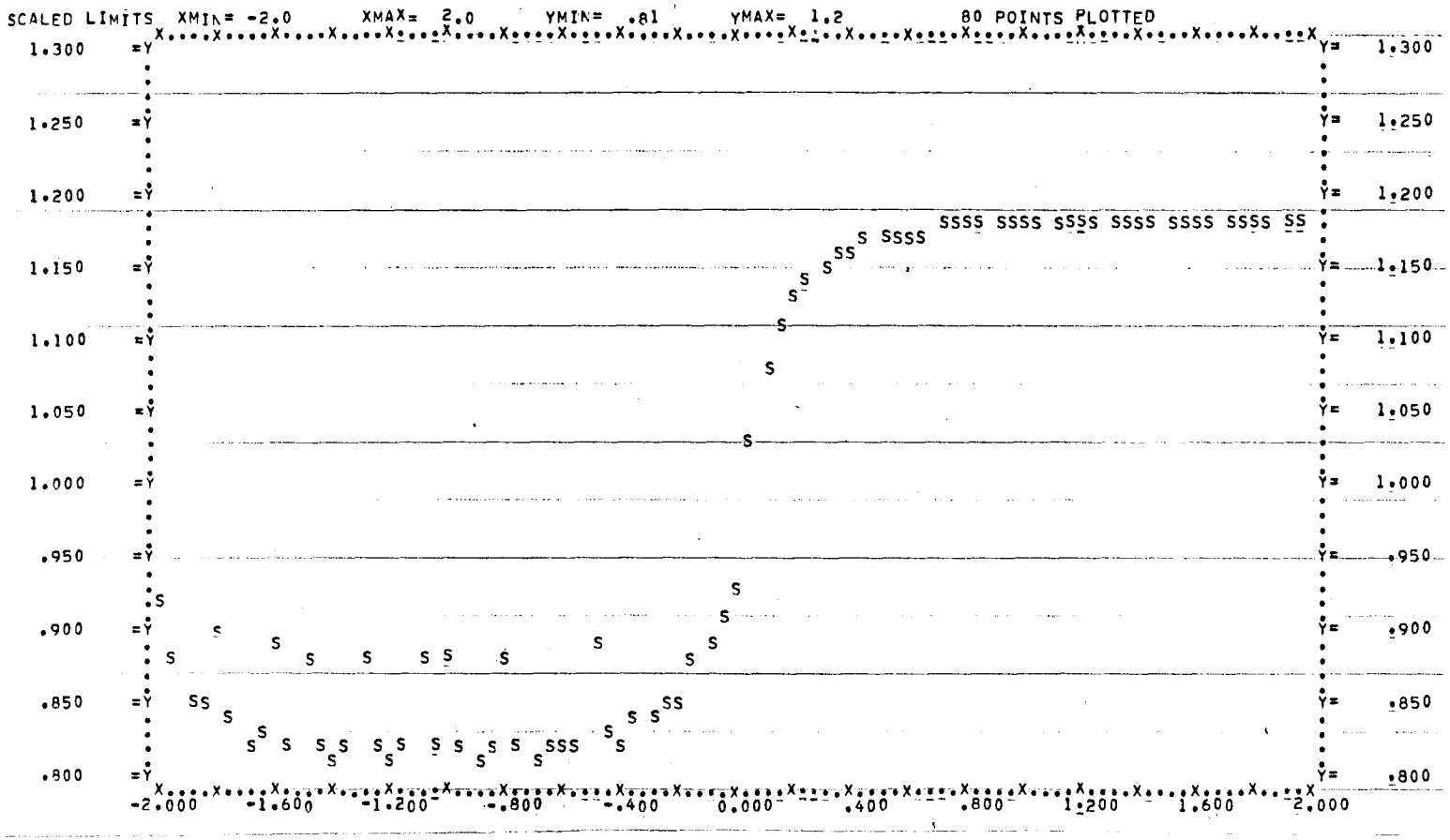

Fig. 4.2(a): Graphic computer output of the flux shape for 1.2 cm thick lucite sample, using the single scattering model.

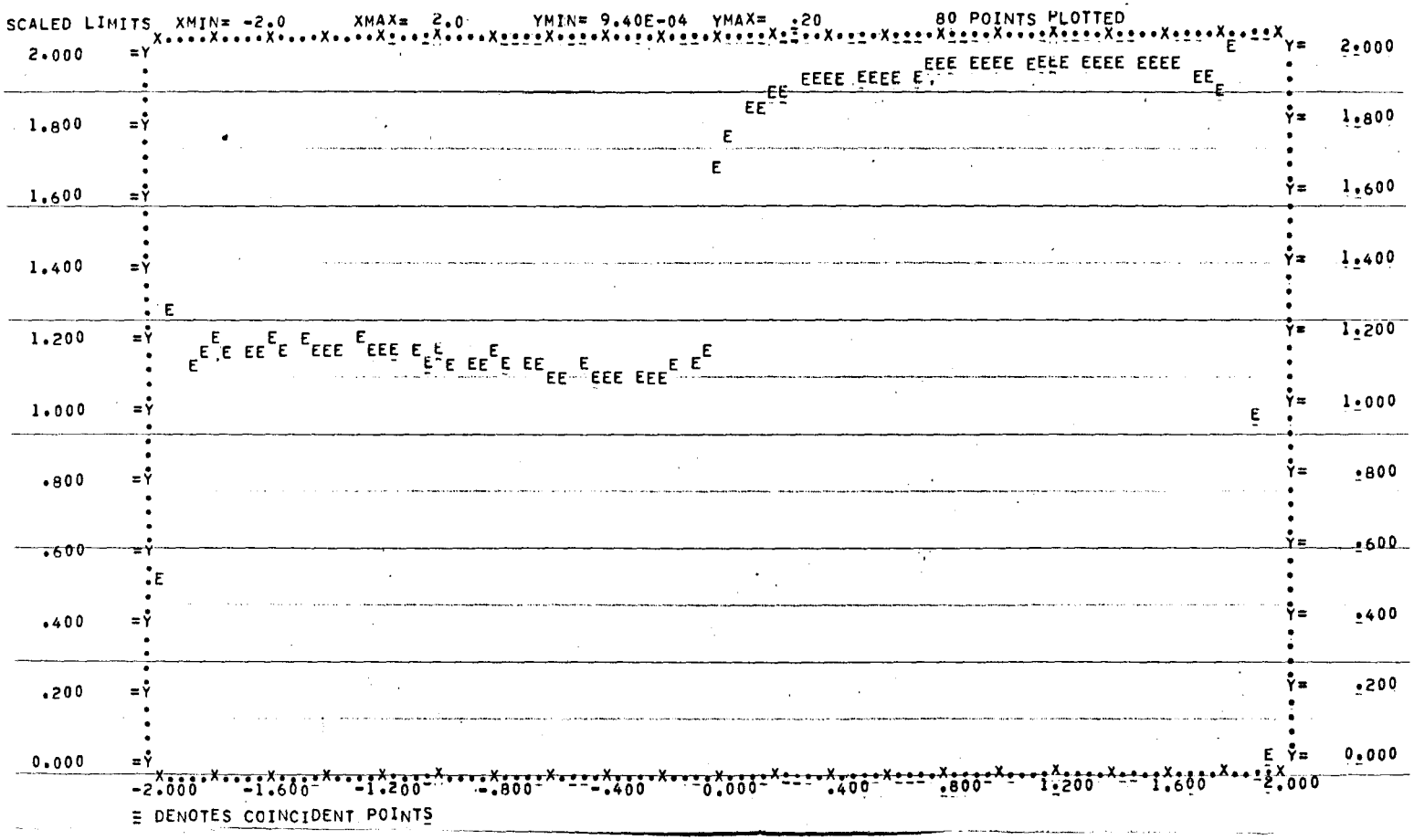

Fig. 4.2(b): Graphic computer output showing the optical density for 1.2 cm thick lucite sample.

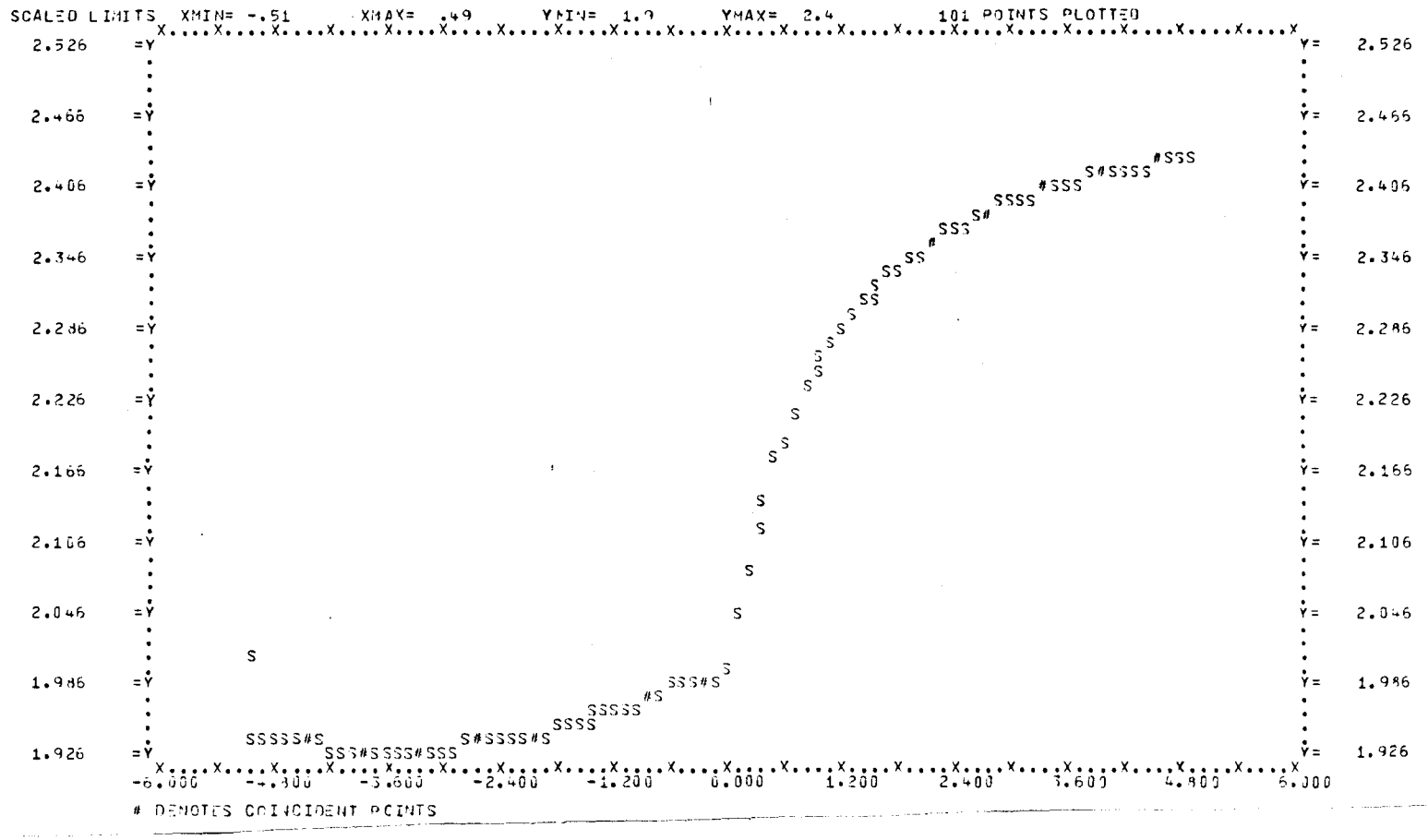

Fig. 4.3(a): Flux shape obtained for only a few mm across 1.2 cm thick lucite knife edge sample, using a more refined mesh.

Fig. 4.3(b): The optical density obtained for only a few mm across the 1.2 cm thick lucite knife edge sample.

CHAPTER 5

COMPARISON OF THEORETICAL AND EXPERIMENTAL RESULTS

The results obtained from the single scattering model are compared graphically with experimental results by plotting the normalised optical density in each case, against the spatial coordinates, a few millimeters across the sample edge. Since the optical density scans obtained from the microdensitometer lies between -1.0 mm to +1.0 mm across the sample edge, this aparently defines our region of interest; and we therefore require to obtain sufficient number of points to be plotted within this small interval in our theoretical calculation. A minimum reasonable step length for our mesh points may be taken as 0.1 mm. We also require the integration of the flux with the Lorentzian function, to cover enough distance across the edge which contributes to the optical density measured about the edge; but in practice, it is very expensive even to integrate from -2.0 cm to +2.0 cm across the edge, which will correspond to 400 mesh points. This means that considering a sample thickness of 1 cm and using a step length of only 1 mm, a total of 10 mesh points to cover the thickness, we will require to perform a total of 4000 integrations.

Indeed, the above is about the number of integrations performed for each of the theoretical results we are about to compare with experimental results. From the above economic considerations, we cannot afford to carry out the optimum number of integrations required for the best results.

Another factor which affects our theoretical results is the choice of the Lorentzian coefficient C_L, which is not precisely

known for this radiographic system involving lucite samples. The value of $C_L = 6 \times 10^3$ cm^{-2} used, was only chosen from a number of trial values. We shall see shortly how the value of C_L affects our result.

Inspite of the above limitations, the comparisons shown in Fig. 5.1 - Fig. 5.5 can be best described as satisfactory. The comparisons between experiment and theory have been made for various thicknesses of 0.5 cm, 0.7 cm, 1.0 cm and 1.2 cm lucite samples. The general trend in the comparison shows that we have more optical density at the toe and less optical density at the hill in our theoretical results.

By increasing the value of C_L, the theoretical optical density will be reduced, since in the calculation, C_L appears in the denominator. This is actually the case as shown in Fig. 5.5 with C_L increased by a factor of 10 to 6×10^4 cm^{-2} for 1.2 cm sample thickness. The decrease in optical density due to increase in C_L gives a very good fit at the toe of the curves as shown in Fig. 5.5, but makes the theoretical optical density even lower at the hill of the curves. This suggests that if we require any improvement in our results, and assuming that the best value of C_L is known, we will have to resort to the following - refine the integration mesh and increase the range of integration and/or include some build-up factor in our analysis.

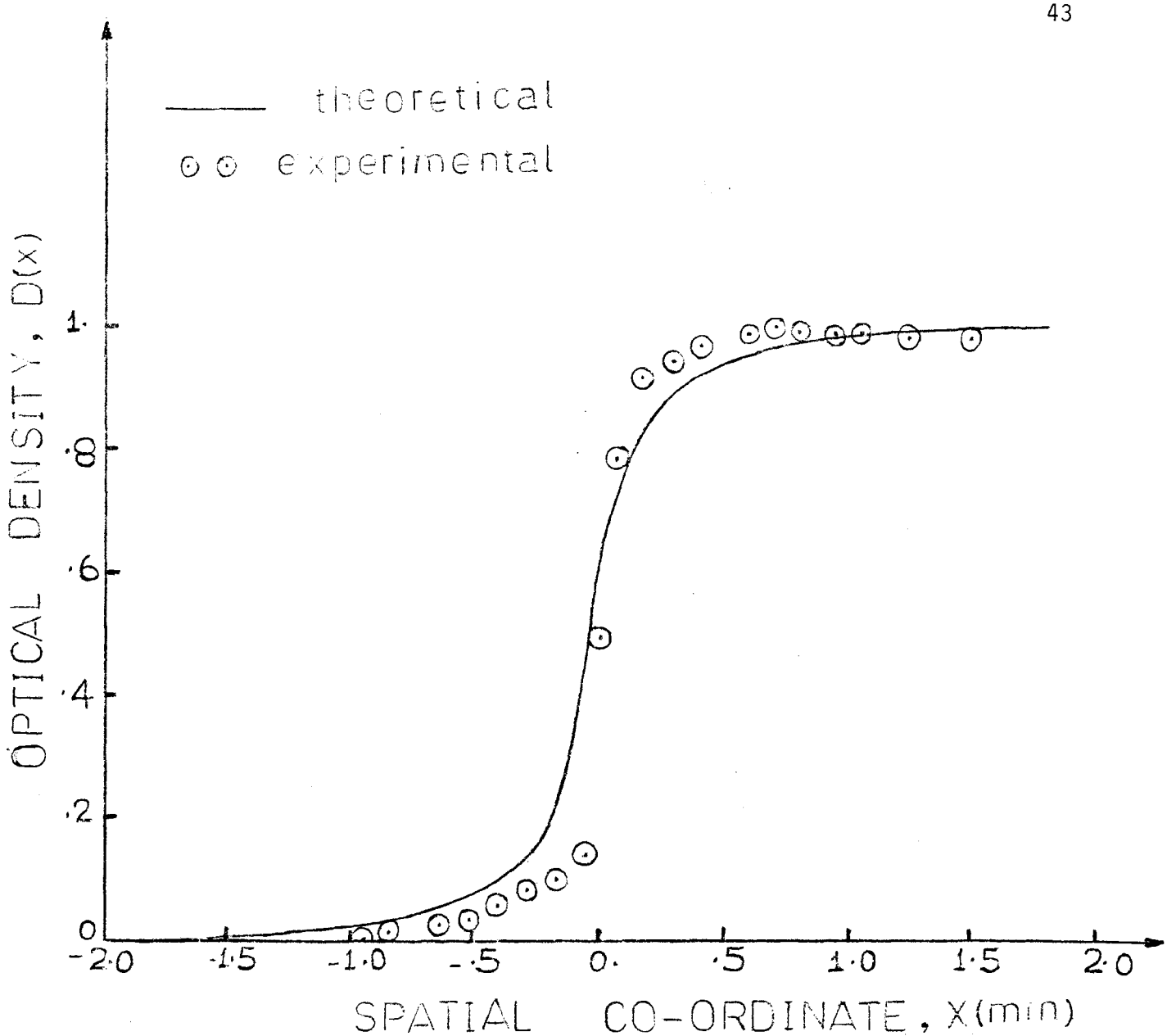

Fig. 5.1: Experimental and theoretical curves for 0.5 cm thick lucite sample, with $C_L = 6 \times 10^3$ cm^{-2}.

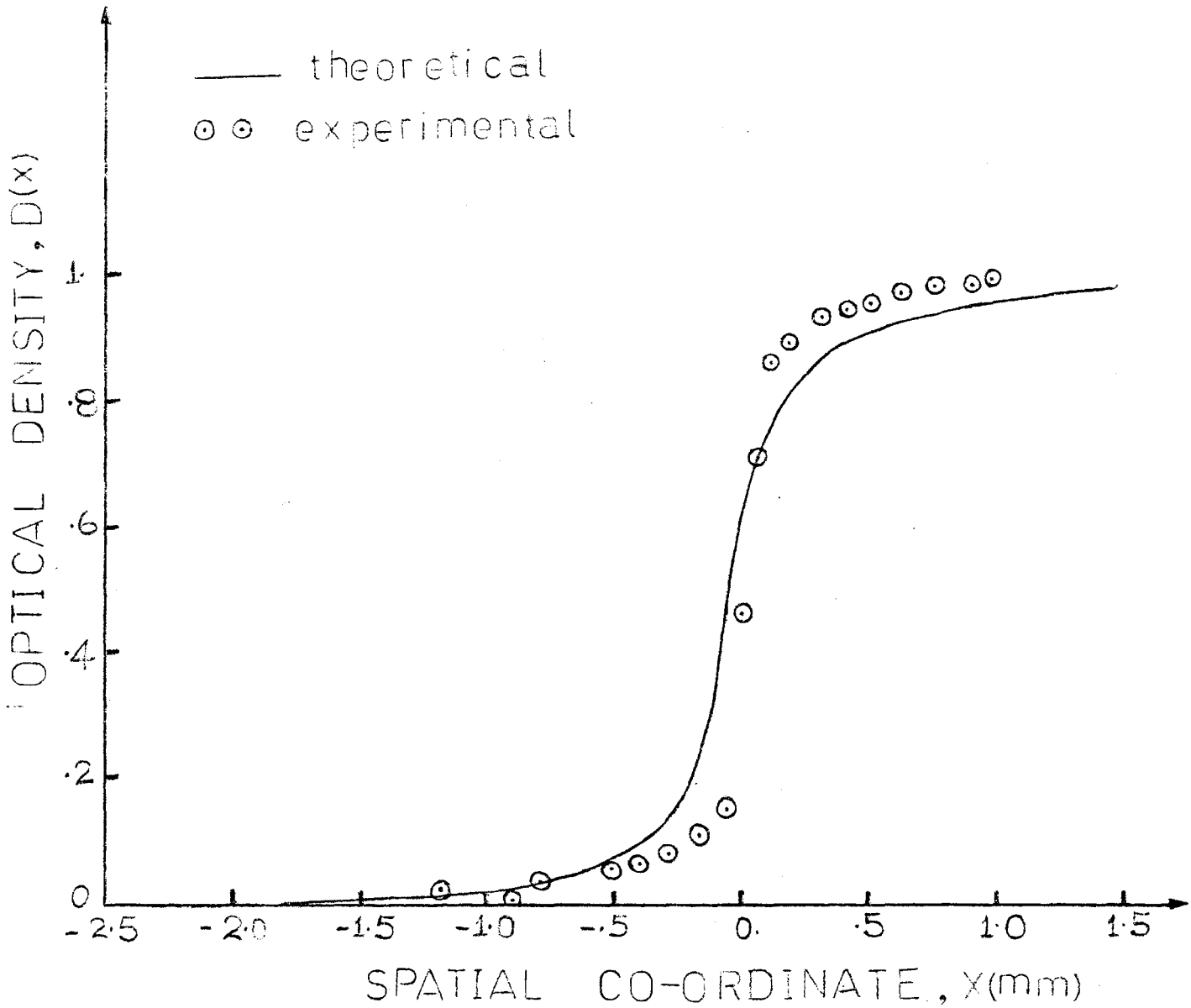

Fig. 5.2: Experimental and theoretical curves for 0.7 cm thick lucite sample, with $C_L = 6 \times 10^3$ cm^{-2}.

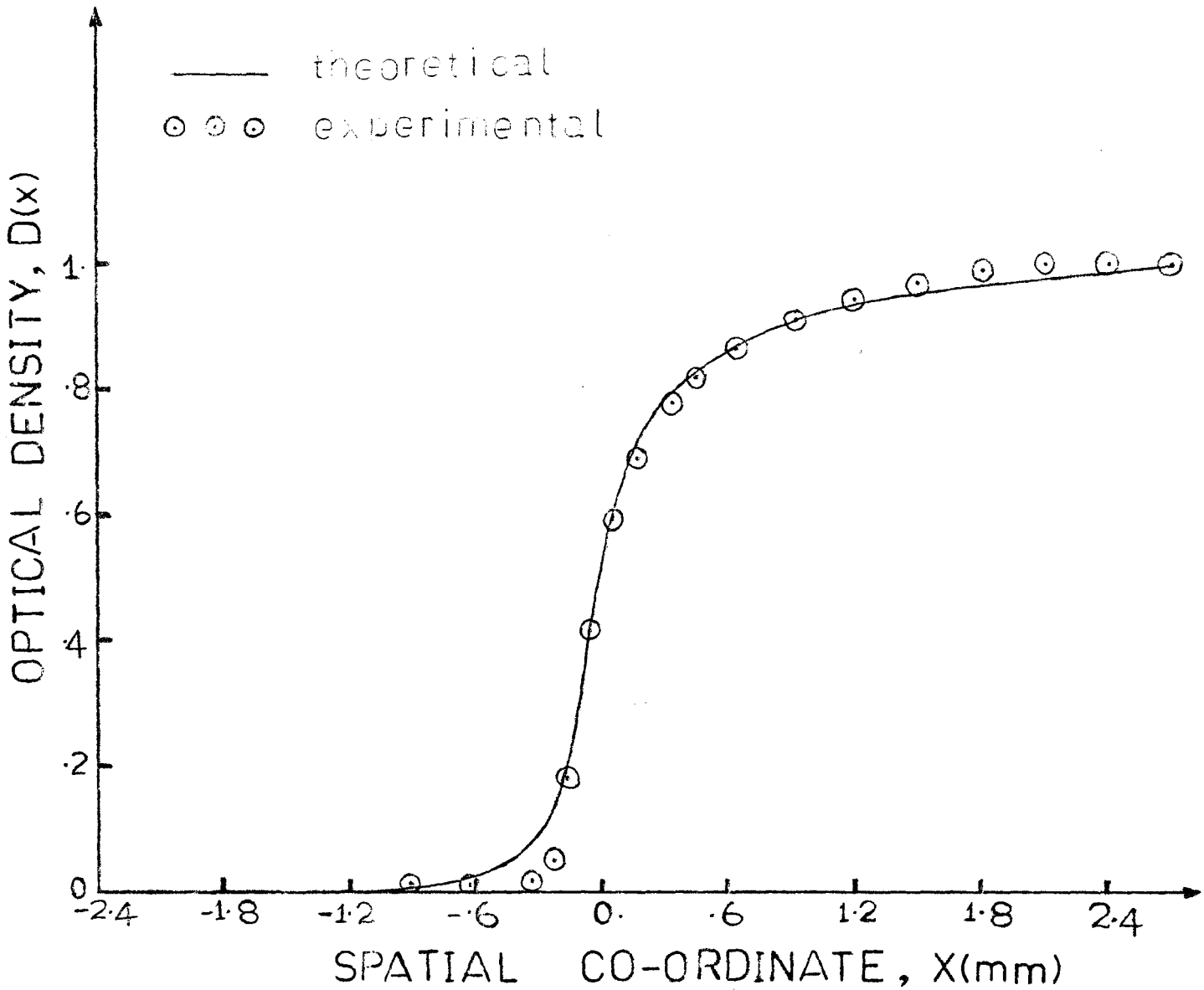

Fig. 5.3: Experimental and theoretical curves for 1.0 cm thick lucite sample, with $C_L = 6 \times 10^3$ cm^{-2}.

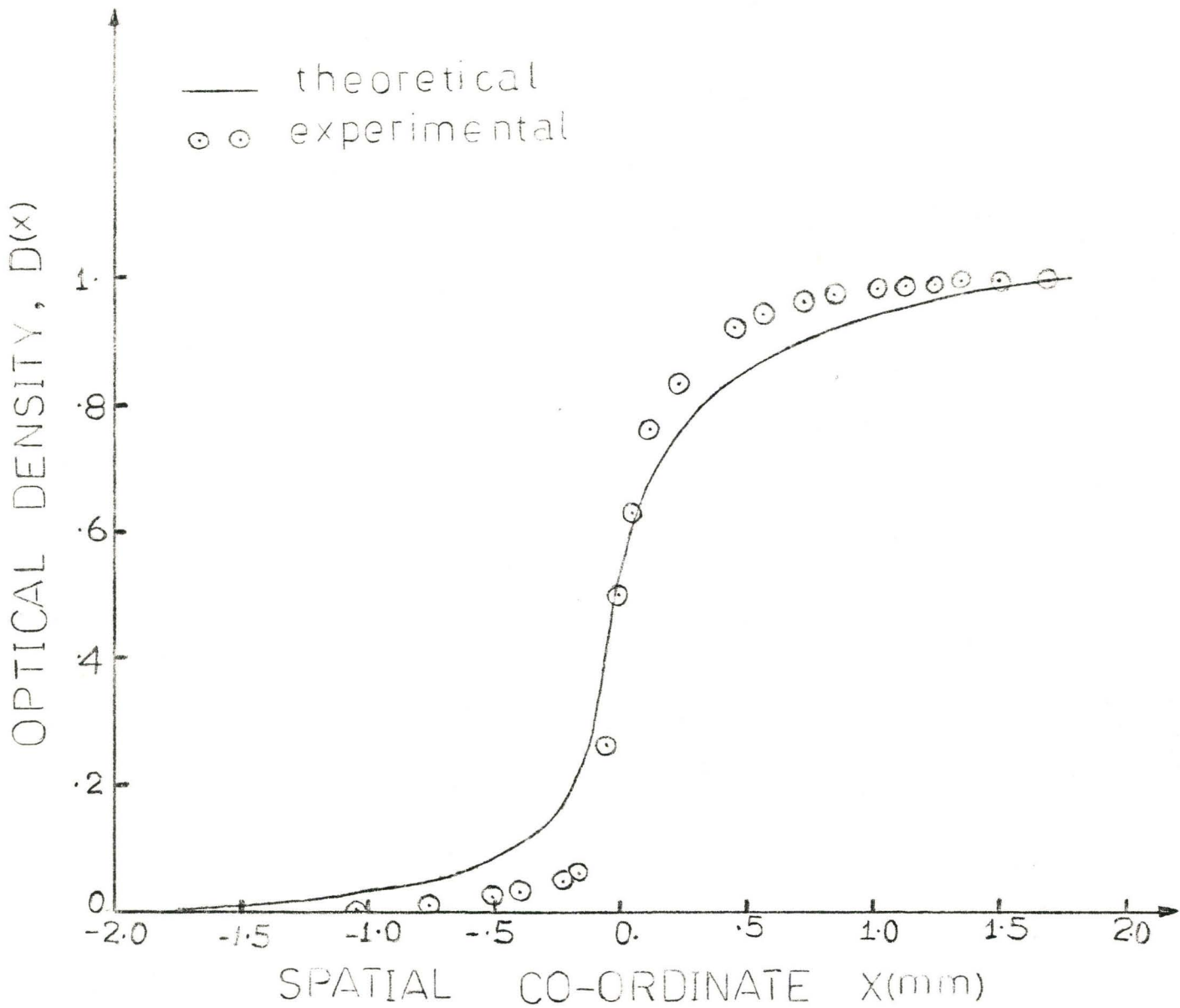

Fig. 5.4: Experimental and theoretical curves for 1.2 cm thick lucite sample, with $C_L = 6 \times 10^3$ cm^{-2}.

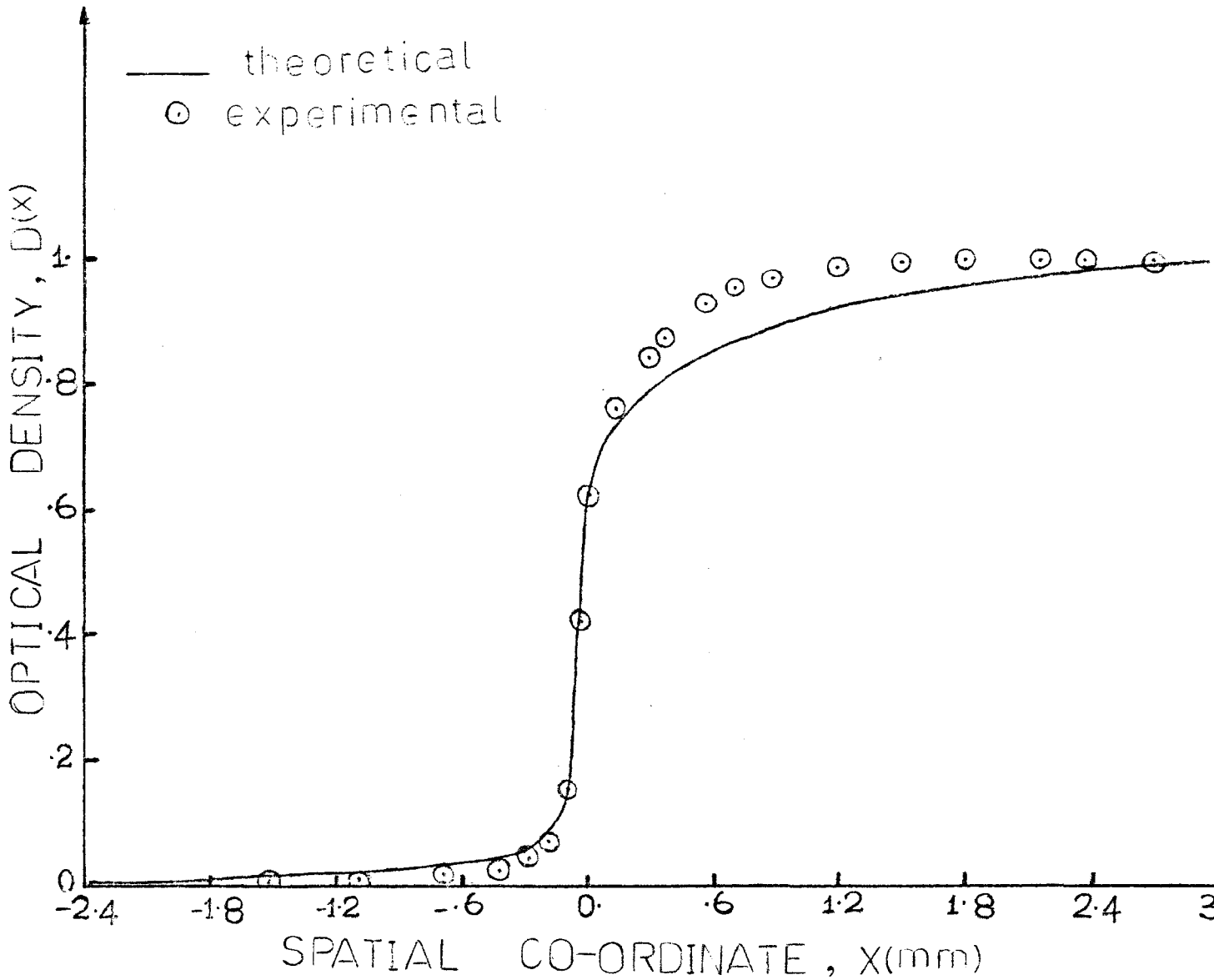

Fig. 5.5: Experimental and theoretical curves for 1.2 cm thick lucite sample, with $C_L = 6 \times 10^4$ cm^{-2}.

CHAPTER 6

PROPOSAL FOR GENERALIZED LORENTZIAN ANALYSIS

The detailed integral analysis described in the preceeding chapters is both tedious and expensive to use for regular radiographic work. In this chapter, we propose a generalized Lorenzian function and explore its possibilities as an alternative method for analysis.

On the basis of the symmetric Lorentzian function, we propose a generalized Lorentian function of the form

$$L_G(\xi, C_i) = \frac{1}{\sum_{i=o}^{N} C_i \xi^i} \quad ; \quad C_o = 1 \tag{6.1}$$

For the case of N = 2 we have

$$L_G(x, C_1, C_2) = \frac{1}{1 + C_1 X + C_2 X^2} \tag{6.2}$$

Equation (6.2) reduces to the familiar Lorentzian function when the odd term in the denominator is set to zero. The inclusion of this odd term will produce a non-symmetric effect to an extent determined by the values of the coefficients C_1 and C_2. In principle therefore, we can obtain a more pronounced non-symmetric effect for the case N = 3 with

$$L_G(x, C_1, C_2, C_3) = \frac{1}{1 + C_1 X + C_2 X^2 + C_3 X^3} \tag{6.3}$$

or retaining, for simplicity, only one non-symmetric term we have

$$L_G(x,C_2,C_3) = \frac{1}{1 + C_2X^2 + C_3X^3} \tag{6.4}$$

The above non-symmetric Lorentzian function can be substituted in the general relation

$$S(x,u) = \int \phi(u)L(x,u)du \tag{6.5}$$

The difference in this case as compared to the single scattering approach is that the contribution to non-symmetry is now born by the Lorentzian function and not by the flux reaching the converter. Since we now seek to find a Lorentizan function which accounts for the scattering, the flux will be considered to be constant and equal to unity.

Using the Lorentzian function of Eq. (6.2) we obtain a non-symmetric edge spread function given by

$$S_N(x,C_1,C_2) = \int_{-\infty}^{X} \frac{d\xi}{1 + C_1\xi + C_2\xi^2} \tag{6.6}$$

We shall now initiate a numerical test for Eq. (6.6) to determine how close we are to our goal. Analytically, Eq. (6.6) can be reduced to the closed form

$$S_N(x,C_1,C_2) = \begin{cases} \dfrac{2}{\sqrt{(4C_2-C_1^2)}} \tan^{-1}\left\{\dfrac{2C_2X + C_1}{\sqrt{(4C_2-C_1^2)}}\right\}, & [4C_2 > C_1 2] \\ \dfrac{1}{\sqrt{(C_1^2-4C_2)}} \log\left|\dfrac{2C_2X+C_1-\sqrt{(C_1^2-4C_2)}}{2C_2+C_1+\sqrt{(C_1^2-4C_2)}}\right|, & [C_1^2 > 4C_2] \\ \dfrac{1}{\sqrt{(C_1^2-4C_2)}} \tanh^{-1}\left\{\dfrac{2C_2X + C_1}{\sqrt{(C_1^2-4C_2)}}\right\}, & [C_1^2 > 4C_2, (2C_2X+C_1)^2 > C_1^2-4C_2] \end{cases} \quad (6.7)$$

For the present analysis we choose

$$S_N(X,C_1,C_2) = \frac{2}{\sqrt{(4C_2-C_1^2)}} \tan^{-1}\left\{\frac{2C_2X + C_1}{\sqrt{(4C_2-C_1^2)}}\right\}, [4C_2 > C_1^2] \quad (6.8)$$

A curve fitting to Eq. (6.8) can now be performed to develop a feel for this approach.

In Fig. 6.1 and Fig. 6.2 we show some of the results for the curve fitting. The symbol E denotes the experimental curve and F for the fitted curve. As we would expect, the shape of the fitted curve is determined by the values of the coefficients C_1 and C_2. For the fitted curve of Fig. 6.1 $C_1 = .167957 * 10^{-2}$ and $C_2 = 0.1 \times 10^{-4}$ μm^{-2} and for Fig. 6.2 $C_1 = -.018799$, $C_2 = .9999 * 10^{-4}$ μm^{-2}.

Though none of the two curves yields a thorough fit, the former appears satisfactory in the upper half while the later gives a fairly good shape at the lower half. A combination of the two fitted curves, with the upper half of Fig. (6.1) superimposed on the lower half of Fig. (6.2) can lead to a logical satisfactory result as this would imply using different values of the coefficients C_1 and C_2 inside and outside the material region in other to account for the scattering effect.

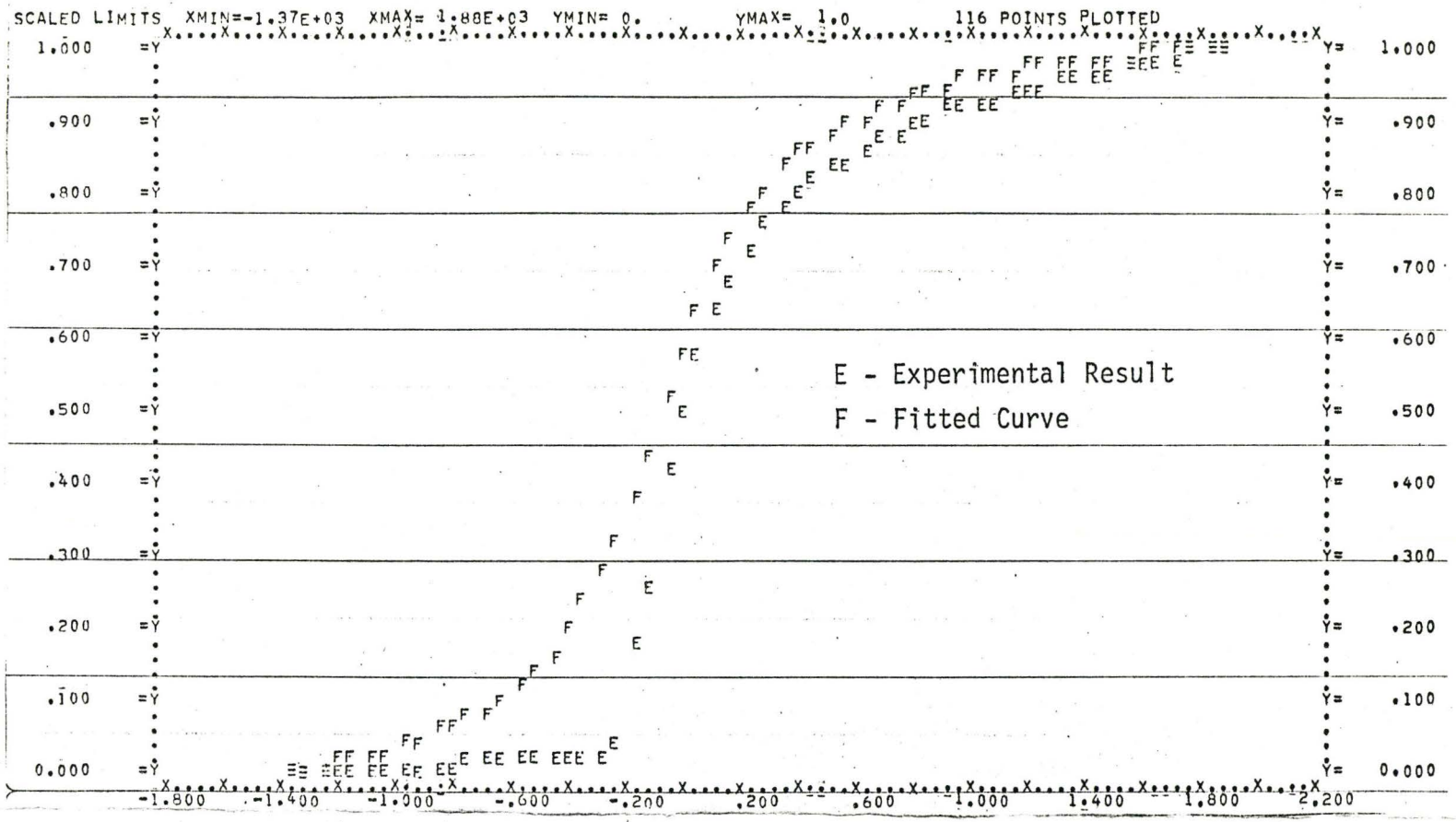

Fig. 6.1: Result of curve fitting to Eq. (6.8) with $C_1 = .1679 \times 10^{-2}$ and $C_2 = .100 \times 10^{-4}$ μm.

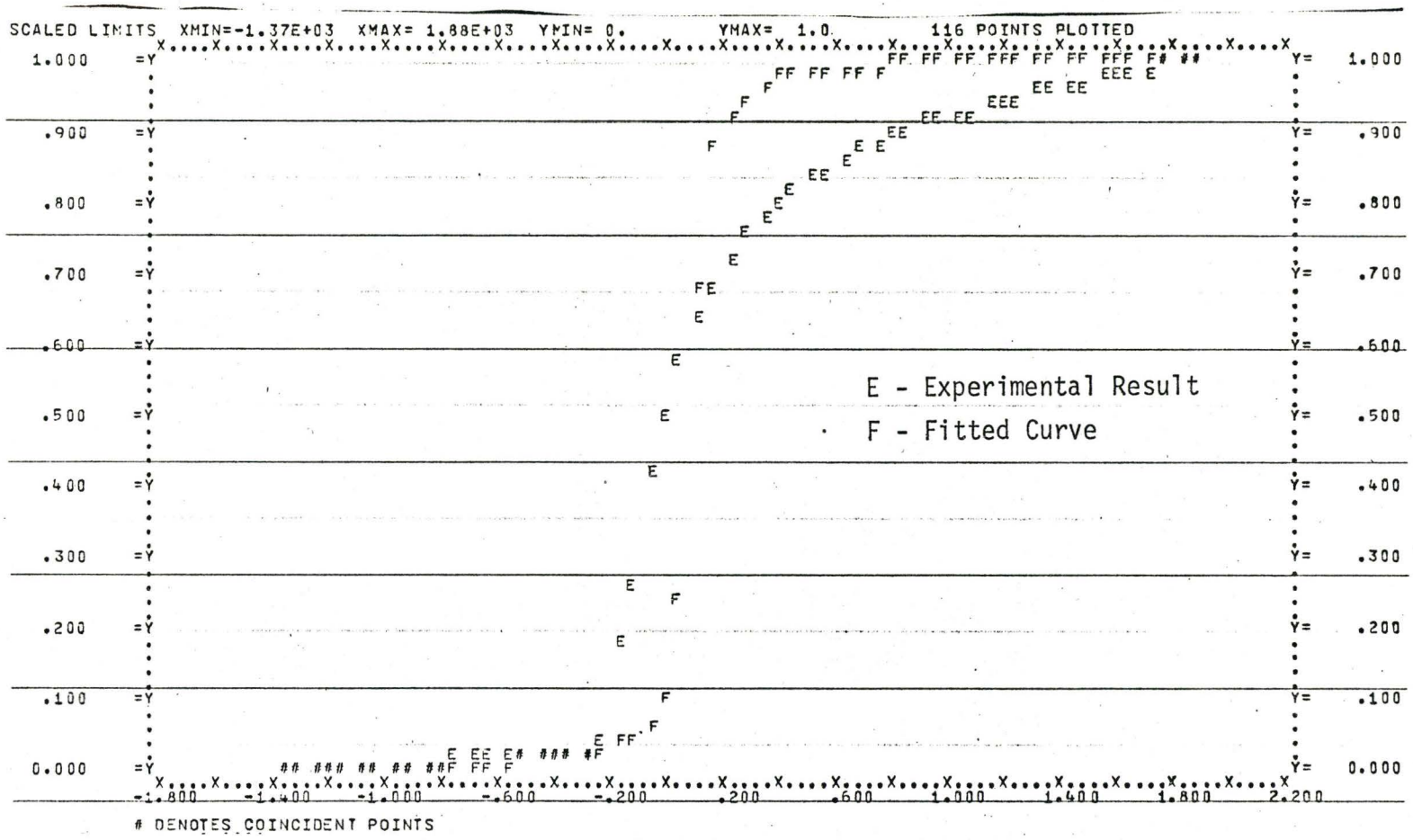

Fig. 6.2: Result of curve fitting to Eq. (6.8) with C_1 = -.01879 and C_2 = .9999 x 10^{-4} μm.

CHAPTER 7

CONCLUSION

The results of the single scattering model give a satisfactory account of the scattering effect on the edge spread function.

In addition to obtaining the required non-symmetric edge spread function, the intermediate theoretical result for the flux shape gives an expository description of the material response as dinstinct from the converter response; the variation of this flux with sample thickness provides an interesting area for further studies.

It is remarkable to observe that the flux shape takes the form of the optical density which conforms to the direct proportionality between the converter response and the flux reaching the converter for the case of linear response region of the film.

The good agreement between theory and experiment suggests that the inclusion of build up factor in the analysis will produce the effect of increasing the flux reaching the converter without changing the flux shape; however, a numerical test for this is another area for further investigation. On the other hand, an accurate value of the Lorentzian coefficient, C_L, combined with optimum mesh intervals will lead to very satisfactory results. It may also be worth while to explore further, the shielding concept appraoch.

The proposed generalized Lorentzian function holds a promising alternative in terms of it's simpler form and reduced computer time but it obvoiusly requires further investigation.

APPENDIX

PROGRAM LISTINGS FOR THE COMPUTER CODE NEUT77

```
      PROGRAM NEUT77(INPUT,OUTPUT,TAPE5=INPUT,TAPE6=OUTPUT)
      DIMENSION X(100),Y(100),SI(500),U(500)
      DIMENSION PHI(500),X1(500),F(500),BPAR(4),C(399,3),Q(500)
      DIMENSION FF(13,33),WK(845)
      DIMENSION X2(500),Q2(500),U2(500),S2(500)
      DIMENSION X0(400),Q0(400),X22(100),Q22(100)
      DIMENSION DIST(64),SLOPE(64),XX(200),QQ(200)
      DIMENSION XE(100),DE(100),XXE(100),DDE(100)
      DO 444 L=1,81
  444 READ(5,*)XE(L),DE(L)
      DO 555 K=1,81
      XE(K)=.00564*XE(K)
      DE(K)=DE(K)/38.0
  555 CONTINUE
      A1=-1.9
      B2=2.
      C1=1.E+6
      IC=399
      NX=400
      A=3.9
      YL=1.3
      IX=33
      IY=13
      IU=400
      M=IU+1
      N=13
      DO 111 K=1,4
  111 BPAR(K)=0.
      SIGMA=.2429
      DO 110 K=1,IU
      U(K)=-2.+.01*FLOAT(K)
      DO 220 J=1,IY
      Y(J)=FLOAT(J)/10.
      DO 330 I=1,IX
      X(I)=FLOAT(I)/10.
      R=SQRT((X(I)-U(K))**2+(YL-Y(J))**2)
      IF(U(K).GT.0.)GO TO 12
      R2=R*X(I)/(X(I)-U(K))
      RR=SQRT(1.+((YL-Y(J))/(X(I)-U(K)))**2)
      SJAC=ABS(X(I)/R-U(K)*RR/(X(I)-U(K)))
      GO TO 99
   12 IF(U(K).GT.2.)GO TO 23
      IF(X(I).NE.U(K))GO TO 44
      FF(J,I)=EXP(-SIGMA*YL)
      GO TO 330
   44 R2=R
      RR=SQRT(1.+(YL-Y(J))**2/(X(I)-U(K))**2)
      SJAC=1./RR
      GO TO 99
   23 R2=(A-X(I))*R/(U(K)-X(I))
      RR=SQRT(1.+((YL-Y(J))/(X(I)-U(K)))**2)
      SJAC=ABS((A-X(I))/R-(U(K)-A)*RR/(U(K)-X(I)))
   99 FF(J,I)=EXP(-SIGMA*(Y(J)+R2))*SJAC
  330 CONTINUE
  220 CONTINUE
      SI(K)=OCS20U(FF,Y,X,IY,IX,N,WK,IER)
  110 CONTINUE
```

```
      DO 144 K=1,IU
      U2(K)=-U(M-K)
      S2(K)=SI(M-K)
  144 CONTINUE
      DO 232 L=150,250
      WRITE 100,U2(L),S2(L)
      CALL PLOTPT(U2(L),S2(L),39)
  232 CONTINUE
  100 FORMAT(10X,2E12.4)
      CALL OUTPLT
      DO 88 I=1,200
   88 PHI(I)=1.+SI(I)
      DO 55 I=201,400
   55 PHI(I)=SI(I)
      DO 155 J=1,400
      X1(J)=-2.+.01*FLOAT(J)
      DO 166 K=1,400
  166 F(K)=PHI(K)/(1.+C1*((X1(J)-U(K))**2))
      CALL ICSICU(U,F,NX,BPAR,C,IC,IER)
      CALL DCSQDU(U,F,NX,C,IC,A1,B2,Q(J),IER)
  155 CONTINUE
      DO 177 J=1,IU
      X2(J)=-X1(M-J)
      Q2(J)=Q(M-J)
  177 CONTINUE
      DO 343 L=150,250
      WRITE 501,X2(L),Q2(L)
      CALL PLOTPT(X2(L),Q2(L),25)
  343 CONTINUE
  501 FORMAT(2X,2E12.4)
      CALL OUTPLT
      DIFF=Q2(231)-Q2(177)
      DO 202 K=177,231
      X2(K)=25.*X2(K)
      Q2(K)=10.*(Q2(K)-Q2(177))/DIFF
  202 CONTINUE
      XSCALE=.04
      YSCALE=.1
      V=-.44
      W=-.5
      XMIN=-.44
      XMAX=.4
      YMIN=-.5
      YMAX=1.5
      CALL PLOT(1.,1.,-20)
      CALL LETTER(6,.5,90.,1.,5.,5HOSUWA)
      CALL PLOT(0.,0.,-3)
      CALL PLTIN(XSCALE,YSCALE,V,W,XMIN,XMAX,YMIN,YMAX)
C     PLOT THE AXES
      CALL PLOT(5.,4.,3)
      CALL PLOT(26.,4.,2)
      CALL PLOT(5.,16.,3)
      CALL PLOT(5.,4.,2)
C     LABEL AXES
      CALL LETTER(21,.3,90.,4.,6.,20HOPTICAL DENSITY,D(X))
      CALL LETTER(26,.3,0.,8.,3.,25HSPATIAL CO-ORDINATE,X(CM))
C     PLOT CURVE

      CALL DDASHM(X2,Q2,55,1.,0.,0.,1.,.2,IE,DIST,SLOPE)
      CALL PLOT(0.,0.,-3)
      NN=81
      DO 606 J=1,NN
  606 CALL UNITTO(XE(J),DE(J),XXE(J),DDE(J))
C     PLOT CURVE
      CALL PLOT(XXE(1),DDE(1),3)
      DO 808 M=2,NN
      CALL PLOT(XXE(M),DDE(M),2)
  808 CONTINUE
      CALL PLOT(50.,0.,-3)
      CALL PLOT(50.,0.,999)
      STOP
      END
```

REFERENCES

1. HARMS, A.A., HEINDLER, M., BURNS, D.M., "Accurate Dimensional Measurement in Neutron Radiography", Materials Evaluation, 36 (5), 49 (1978).
2. HARMS, A.A., ZIELINGER, A., "A New Formulation of Total Unsharpness in Radiography", Phys. Med. Biol., 22, 70 (1977).
3. IMSL LIBRARY 43.01 ba, McMaster University, "DCS2QU - Two Dimensional Cubic Spline Quadrature".
4. HARMS, A.A., "Recent Theoretical-Experimental Correlations in Neutron Radiographic Imaging", Proc. BNES Conf.: Radiography with Neutrons, University of Birmingham, Sept. 10-11, 1973.
5. GARSIDE, B.K., HARMS, A.A., "Detection Process in Neutron Radiography", J. Appl. Physl, 42 (12), (1971).
6. BUTLER, M.P., "Studies in Neutron Radiography", Variation of Lorentzian Coefficient with Material and Thickness, Eng. Physics Dept., McMaster University (unpublished).
7. ROBERTSON, T.J.M., "Neutron Radiography in the Precision Measurement of Irradiated Materials", Proceedings NBES Conference on Radiography with Neutrons, University of Birmingham, U.K., 10-11 September, 1973, British Nuclear Energy Society, London, 1975.
8. DOMANUS, J.C., "Accuracy of Dimension Measurements from Neutron Radiographs of Nuclear Fuel Pins", Proceedings Eight World Conference on Non-Destructive Testing, Cannes, France, 6-11 September, 1976.
9. OKAWARA, G.S., HARMS, A.A., "Neutron Radiography of Fast Transient Processes", Nucl. Technology, 31, 251 (1976).
10. CUTFORTH, D.C., "Dimensioning Reactor Fuel Specimen from Thermal Radiographs", Nucl. Tech. 18, 67 (1973).